



Optimal Control of a Wheeled Mobile Cable-Driven Parallel Robot ICaSbot with Viscoelastic Cables

Moharam Habibnejad Korayem^{†*},
Mahdi Yousefzadeh[‡] and Hami Tourajizadeh[¶]

[†]*Robotic Research Laboratory, Center of Excellence in Experimental Solid Mechanics and Dynamics, School of Mechanical Engineering, Iran University of Science and Technology, Tehran, Iran*

[‡]*Mechanical Engineering Department, Mazandaran University of Science and Technology, Babol, Iran. E-mail: ma.yousef@gmail.com*

[¶]*Mechanical Engineering Department, Faculty of Engineering, Kharazmi University, Tehran, Iran. E-mail: Tourajizadeh@khu.ac.ir*

(Accepted October 19, 2019. First published online: November 14, 2019)

SUMMARY

In this paper, a new mobile cable-driven parallel robot is proposed by mounting a spatial cable robot on a wheeled mobile robot. This system includes all the advantages of cable robots such as high ratio of payload to weight and good stiffness and accuracy while its deficiency of limited workspace is eliminated by the aid of its mobile chassis. The combined system covers a vast workspace area whereas it has negligible vibrations and cable sag due to using shorter cables. The dynamic equations are derived using Gibbs–Appell formulation considering viscoelasticity of the cables. Therefore, the more realistic viscoelastic cable model of the robot reveals the system flexibility effect and shows the requirements needed to control the end-effector in the conditions with cable elasticity. The viscoelastic system stability is investigated based on the input–output feedback linearization and using only the actuators feedback data. Feedback linearization controller is equipped by two additional controllers, that is, the optimal controller based on Linear Quadratic Regulator (LQR) method and finite horizon model predictive approach. They are used to control the system compromising between the control effort and error signals of the feedback linearized system. The applied control input to the robot plant is the voltage signal limited to a specified band. The validity of modeling and the designed controller efficiency are investigated using MATLAB simulation and its verification is accomplished by experimental tests conducted on the manufactured cable robot, ICaSbot.

KEYWORDS: Cable-driven parallel robot; Wheeled mobile robot; Gibbs–Appell; Non-holonomic; Feedback linearization; LQR.

1. Introduction

Development of the automation and robotic systems in industry is fastly increasing nowadays, especially for load-carrying purposes. In this regard, many researchers are working on different aspects of wheeled mobile robots (WMRs) equipped by manipulator arms. Korayem et al. introduced a method to derive the dynamic equations of a system combined of a WMR and n viscoelastic serial links.¹ They also accomplished path planning of a WMR with two manipulator arms.² The desired path of the platform is obtained based on the desired path of the arms' end-effector, while the dynamic load-carrying capacity is increased by reducing the norm of the control efforts.

* Corresponding author. E-mail: hkorayem@iust.ac.ir

A few researchers proposed the idea of the robotic configuration combining a WMR and a parallel robot. Fujita et al. introduced the design of a parallel manipulator on a rotary link mounted on a WMR for pick and place applications.³ They studied the kinematics as well the singularity issues of the system. In ref. [4], Moosavian et al. proposed the design of a hybrid serial–parallel WMR. They presented the kinematics, dynamics, and stability analysis of the mentioned system. They showed using a parallel planar mechanism to move a serial manipulator's base, the stability can be increased while handling heavy objects. Liu et al. studied the dynamic interaction of two parts of a FAST radio telescope, including a flexible cable-driven parallel robot (CDPR) and a rigid Stewart parallel mechanism by introducing a new index.⁵

The CDPR is a type of parallel robots, in which the links are replaced with cables connecting the electric motors to the end-effector. It benefits from high payload to weight ratio and low-energy consumption as well as simple manufacturing technology. These advantages cause them to be an appropriate choice for handling the objects in a large workspace. However, replacement of the rigid link with the cables results in a more flexible structure. Furthermore, in the workspace condition of low height to the ground area ratio, the efficiency of the CDPR is reduced. This is because of the increase of the cables tension as well as requiring more powerful motors. As proposed in this paper, the combination of a CDPR and a WMR reduces the required length of the cables to cover a large workspace. Despite the lower flexibility in this hybrid configuration due to the reduction of the cables length, a large area can still be covered because of the mobility of the platform.

Most of the previous control strategies implemented for the CDPRs are limited to the robots with rigid model of the cables. A linear model predictive control is employed in ref. [6] to control large-dimension cable robots at low speeds. In this method, the cable tension limitation is considered in the optimization calculations and results in a better accuracy compared to the conventional controllers such as Proportional+Integrator+Derivative (PID) and Sliding Mode Controller (SMC). This study has not considered the cable elasticity. In some research, the swing of the cable robot is reduced using some control techniques. For example, Hwang et al. have proposed a method for oscillation reduction of an under-actuated cable robot with rigid cable model.⁷ In these kind of systems, the swing of the end-effector is unavoidable as a result of the mechanism under-actuation characteristic. In this research, the end-effector swings are reduced by frequency analysis of the system and employing multimode input shaping technique.

Diao et al. analyzed the vibration of a flexible CDPRs and showed that the transversal motion of the cables has much less effect on the end-effector vibration in comparison with its longitudinal motion.⁸ As a result, the cables can be modeled as a linear spring and the transversal motion of the cables can be neglected. Optimal force distribution is accomplished in ref. [9] for cable robotic crane with flexible cables, considering two longitudinal vibrating modes of the cables. For a 6 degree of freedom (DOF) CDPR with longitudinal elasticity of the cables, Zhang et al. obtained the control signal using delta flatness theory.¹⁰ In ref. [11], Laroche et al. controlled a planar 3 DOF over-constrained CDPR using H-inf method, considering the longitudinal elasticity of the cables. Khosravi et al. modeled the cables of a fully constrained CDPR with linear springs while the stability of the system is then guaranteed using the additional feedback from the cables tension.¹² In ref. [13], in order to control a 6 DOF CDPR by feedback linearization method, the effect of the cables longitudinal vibration on the cables tension is considered. In this research, it is assumed that at each time step the overall dynamic of the robot is negligible compared to its vibrational motion. In a similar research, sliding mode controller and FFT method are employed for solving the PDE of cables' vibration.¹⁴

The idea of a CDPR with moving platform was firstly proposed by NIST.¹⁵ In this regard, Oh et al. presented the idea of a CDPR hung from a helicopter and obtained the dynamic equations and control law of the proposed system.¹⁶ Stabilizing the CDPR is accomplished by a robust controller and two time-scale method. They also derived the dynamic equations of a dual stage CDPR proposed by NIST for the applications of cargo load–unload in the harbors.¹⁷ Sliding mode controller was used for the end-effector tracking in the presence of sea disturbances.

This study presents the dynamic model of the combined interacting systems of a wheeled mobile platform and a CDPR with viscoelastic cables. As a result of this proposed system, not only heavy payloads can be replaced accurately as a result of the used cable robot, but also contrary to cable robots, its corresponding workspace is not limited due to employing a mobile chassis to transfer the robot. Thus, the introduced robotic system combines the advantages of accurate and low inertia links of the CDPR system and the vast workspace area of mobile robots with the suppression of inherent cable vibrations of CDPR systems.

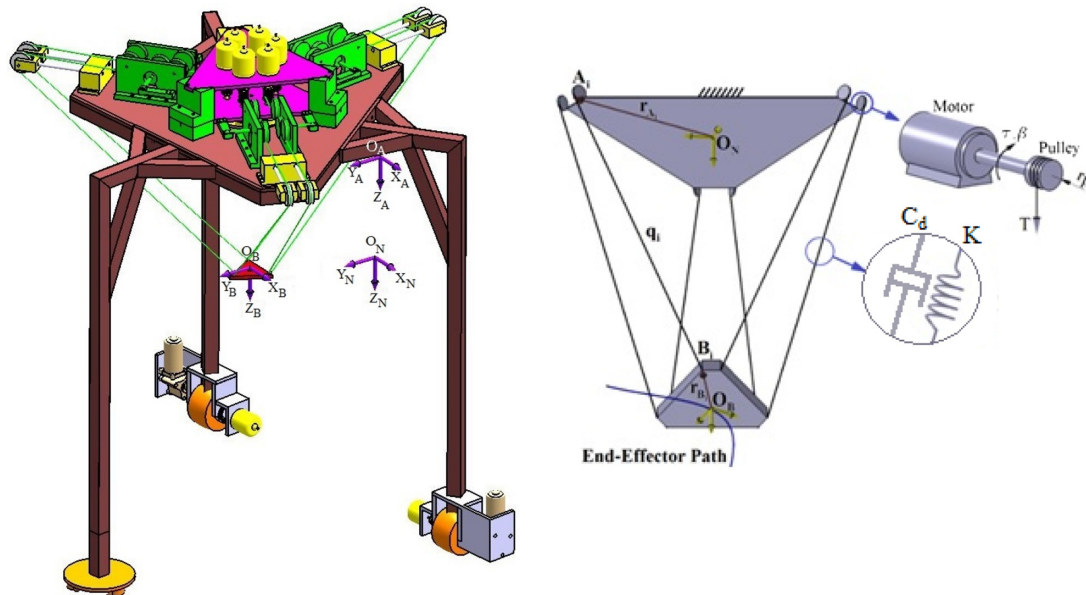


Fig. 1. Schematic view of the wheeled mobile CDPR (left) and schematic view of the platform and the end-effector (right).

It is proven that the control of a CDPR with elastic cables always does not require additional feedback such as cable tension or the direct measurement of the end-effector pose. If a certain cable property exists, the system stability can be assured. Furthermore, the optimal control law for this system is extracted.

This paper is divided into the following sections: in Section 2, the dynamic equations of a 6 DOF CDPR with a wheeled mobile platform are obtained considering viscoelasticity of the cables using Gibbs–Appell method. Then, frequency analysis of the system is performed. Also the stability analysis of the closed loop system is presented in this section. Instead of using the additional feedback from the end-effector pose, which results in the increase of processor computation for control and estimation of the system, only the actuators' feedback is employed in the rigid model-based controller of the flexible model. In Section 3, in order to make a compromise between the control signals and the errors, LQR controller is used to determine the control signal of the outer loop. In addition, in Section 4, combination of Feedback Linearization control and Finite Horizon Model Predictive control (FHMPC) is described to consider the corresponding constraints on the control signal. Simulations in Section 5 include two parts: First, the two described controllers of LQR and FHMPC are compared. Afterwards, the effects of cable elasticity as well as cable sagging due to the cable mass are compared in the end-effector tracking deviation. Since the robot is under-constrained, two main limitations exist. Singularity zones related to the Jacobian matrix of the system and positive tension condition of the cables. It is supposed in this paper that the robot is working within its allowable workspace. In Section 6, the extracted simulation and experimental results are compared and the effectiveness of the proposed model and control approach are shown. The conclusion of the paper is provided in Section 7.

2. Dynamics of the CDPR with Wheeled Mobile Platform and Viscoelastic Cables

2.1. Modeling the system

Figure 1 shows a view of the CDPR with wheeled mobile platform. In this figure, the frames attached to the moving platform and the end-effector are displayed. The triangular end-effector of the robot is moved by six viscoelastic cables with the length-dependent elasticity and damping matrices of \mathbf{K} and \mathbf{C}_d . In this paper, the notation ${}^k x_{mm}$ indicates that the variable x in the frame m is observed from the frame n and is expressed in the frame k . The symbols, A , B denote the frames attached to the platform and the end-effector, respectively, and N is the inertial frame. The center of the coordinate system attached to the end-effector is denoted by O_B , where the center of gravity (C.G.) of the end-effector is located. In the C.G. of the platform, the center of the platform coordinate system, O_A ,

is located. It is assumed that the platform moves on the flat ground without slipping. Pure rolling condition of the wheels results in two non-holonomic and one holonomic constraints.¹⁸ By arranging the constraints in a matrix form, the direct kinematic equation of the platform can be presented as,

$$\dot{\mathbf{x}}_A = \mathbf{C}_6 \dot{\boldsymbol{\theta}} \tag{1}$$

where

$$\mathbf{x}_A = [x_{AN}, y_{AN}, 0, \boldsymbol{\psi}_A^T]^T, \quad \boldsymbol{\psi}_A = [\mathbf{0}_{1 \times 2}, \varphi_A]^T, \quad \boldsymbol{\theta} = [\theta_r, \theta_l]^T,$$

$$\mathbf{C}_6 = \frac{r_{wh}}{2} \begin{bmatrix} \frac{d}{b} \sin \varphi_A + \cos \varphi_A & -\frac{d}{b} \sin \varphi_A + \cos \varphi_A \\ -\frac{d}{b} \cos \varphi_A + \sin \varphi_A & \frac{d}{b} \cos \varphi_A + \sin \varphi_A \\ \mathbf{0}_{3 \times 1} & \mathbf{0}_{3 \times 1} \\ -\frac{1}{b} & \frac{1}{b} \end{bmatrix}$$

The variables $\dot{\theta}_r$, $\dot{\theta}_l$, and $\dot{\varphi}_A$ denote the angular velocities of the right wheel, left wheel, and the platform, respectively. The translational velocities of the platform in the inertial frame are \dot{x}_{AN} and \dot{y}_{AN} . The parameters d , b , and r_{wh} are representation of the distance between Z axis of the platform and the line connecting driving wheels, the half of the distance between wheels, and the radius of the driving wheels, respectively. Note that the Z coordinate of the platform is considered to be zero. The X axis of the platform is perpendicular to the line connecting the wheels and its direction is from the rear wheels toward the front caster wheels. The velocity vector of the end-effector $\dot{\mathbf{x}}_B = [{}^N \dot{\mathbf{x}}_{BN}, {}^B \boldsymbol{\omega}_{BN}]^T$ consists of the translational velocity vector ${}^N \dot{\mathbf{x}}_{BN} = [\dot{x}_{BN}, \dot{y}_{BN}, \dot{z}_{BN}]^T$ and the angular velocity vector ${}^B \boldsymbol{\omega}_{BN} = [{}^B \omega_{BN,x}, {}^B \omega_{BN,y}, {}^B \omega_{BN,z}]^T$ in the inertial frame and the end-effector frame, respectively. Employing the relation between the Euler angles rate and the end-effector angular velocity, the kinematic equation of the end-effector can be expressed as

$$\dot{\mathbf{x}}_B = \mathbf{C}_8 \dot{\boldsymbol{\psi}}_B \tag{2}$$

where

$$\mathbf{x}_B = [{}^N \mathbf{x}_{BN}^T \quad \boldsymbol{\psi}_B^T]^T, \quad \boldsymbol{\psi}_B = [\psi \quad \theta \quad \varphi]^T, \quad \mathbf{C}_8 = \begin{bmatrix} \mathbf{I}_3 & \mathbf{0}_3 \\ \mathbf{0}_3 & \mathbf{P}_B \end{bmatrix}$$

where $\boldsymbol{\psi}_B$ and \mathbf{P}_B are Euler angles vector and Euler angles rate matrix of the end-effector, respectively. The output shaft speed and acceleration of the CDPR's motors can be expressed based on the cables length rate as follows:

$$\dot{\boldsymbol{\beta}} = -\frac{1}{r} \dot{\mathbf{q}} = \frac{1}{r} \boldsymbol{\Lambda}^T \mathbf{A}^T \bar{\mathbf{R}}_B (\mathbf{C}_1 \dot{\mathbf{x}}_A + \mathbf{C}_2 \dot{\mathbf{x}}_B) \tag{3}$$

where $\boldsymbol{\beta} = [\beta_1 \quad \dots \quad \beta_6]^T$, $\dot{\mathbf{q}} = [\dot{q}_1 \quad \dots \quad \dot{q}_6]^T$, $\boldsymbol{\Lambda} = \begin{bmatrix} \dots & -{}^N \mathbf{R}_A^T \mathbf{N} \hat{\mathbf{q}}_i & \dots \\ \dots & -{}^N \mathbf{R}_A^T ({}^N \mathbf{R}_B \mathbf{r}_{Bi} \times \mathbf{N} \hat{\mathbf{q}}_i) & \dots \end{bmatrix}_{6 \times 6}$, $\mathbf{A} \bar{\mathbf{R}}_B = \begin{bmatrix} \mathbf{I}_3 & \mathbf{0}_3 \\ \mathbf{0}_3 & {}^N \mathbf{R}_A^T \mathbf{N} \mathbf{R}_B \end{bmatrix}$ where $\boldsymbol{\beta}$, \mathbf{q} , and $\mathbf{N} \hat{\mathbf{q}}_i$, $i = 1 : 6$ are rotation vector of the CDPR's motors, the vector of the cables length, and the unit vector of the i th cable in frame N, respectively. The cable drum radius is denoted by r . Also, ${}^N \mathbf{R}_j$, $j = A, B$ denotes the rotation matrix of frame j with respect to frame N. The coefficient matrices \mathbf{C}_i , $i = 1 : 5$, are expressed completely in Appendix A. In order to derive the dynamic equations using Gibbs–Appell method, the quasi velocity vector $\boldsymbol{\xi} = [\dot{\mathbf{x}}_B^T \quad \dot{\boldsymbol{\theta}}^T \quad \dot{\boldsymbol{\beta}}^T]^T$ is defined. According to the Appendix B, by substitution of the Gibbs function, generalized power, potential energy rate, and the dissipated energy in the Gibbs–Appell formulation, the dynamic equations can be obtained as follows:

$$[M_B] \ddot{\mathbf{x}}_B + \begin{bmatrix} \mathbf{0}_{3 \times 1} \\ {}^B \boldsymbol{\omega}_{BN} \times \mathbf{I}_B {}^B \boldsymbol{\omega}_{BN} \end{bmatrix} + \begin{bmatrix} \mathbf{0}_{2 \times 1} \\ -m_b g \\ \mathbf{0}_{3 \times 1} \end{bmatrix} - r_p \mathbf{C}_4^T (\mathbf{K} \Delta \mathbf{q} + \mathbf{C}_d \Delta \dot{\mathbf{q}}) = \mathbf{0} \tag{4}$$

$$\begin{aligned}
 & [\mathbf{I}_w + \mathbf{C}_6^T ([M_A] + \mathbf{C}_{10}^T \mathbf{I}_m \mathbf{C}_{10}) \mathbf{C}_6] \ddot{\boldsymbol{\theta}} + \mathbf{C}_6^T \mathbf{C}_{10}^T \mathbf{I}_m \ddot{\boldsymbol{\beta}} + \mathbf{C}_6^T ([M_A] + \mathbf{C}_{10}^T \mathbf{I}_m \mathbf{C}_{10}) \mathbf{C}_7 \dot{\varphi}_A \dot{\boldsymbol{\theta}} \\
 & + \mathbf{C}_6^T \begin{bmatrix} \mathbf{0}_{3 \times 1} \\ \dot{\boldsymbol{\psi}}_A \times \mathbf{I}_A \dot{\boldsymbol{\psi}}_A \end{bmatrix} - r_p (\mathbf{C}_3 \mathbf{C}_6)^T (\mathbf{K} \Delta \mathbf{q} + \mathbf{C}_d \Delta \dot{\mathbf{q}}) = \boldsymbol{\tau}_\theta
 \end{aligned} \tag{5}$$

$$\mathbf{I}_m \ddot{\boldsymbol{\beta}} + \mathbf{I}_m \mathbf{C}_{10} \mathbf{C}_6 \ddot{\boldsymbol{\theta}} + \mathbf{I}_m \mathbf{C}_{10} \mathbf{C}_7 \dot{\varphi}_A \dot{\boldsymbol{\theta}} + \frac{r_p}{2} \text{diag}^{-1}(\mathbf{q}_u) \text{diag}(\mathbf{q} + \mathbf{q}_u) \mathbf{K} \Delta \mathbf{q} + r_p \mathbf{C}_d \Delta \dot{\mathbf{q}} = \boldsymbol{\tau}_\beta \tag{6}$$

where r_p is the radius of the pulley, $\boldsymbol{\tau}_\theta$ and $\boldsymbol{\tau}_\beta$ are the torques of the wheel motors and the CDPR’s motors, respectively. The variable $\Delta \mathbf{q} = \mathbf{q} - \mathbf{q}_u$ is the cable elongation vector due to the cables elasticity, where \mathbf{q} and \mathbf{q}_u are the stretched and unstretched cable length vectors. Due to the small changes of the cables length, the following assumption can be considered:

$$\text{diag}^{-1}(\mathbf{q}_u) \text{diag}(\mathbf{q} + \mathbf{q}_u) \approx 2 \mathbf{I}_6 \tag{7}$$

Therefore, Eq. (6) can be rewritten as:

$$\mathbf{I}_m \ddot{\boldsymbol{\beta}} + \mathbf{I}_m \mathbf{C}_{10} \mathbf{C}_6 \ddot{\boldsymbol{\theta}} + \mathbf{I}_m \mathbf{C}_{10} \mathbf{C}_7 \dot{\varphi}_A \dot{\boldsymbol{\theta}} + r_p (\mathbf{K} \Delta \mathbf{q} + \mathbf{C}_d \Delta \dot{\mathbf{q}}) = \boldsymbol{\tau}_\beta \tag{8}$$

Considering Eqs. (5) and (8), and the equation obtained by multiplying the two sides of Eq. (4) by \mathbf{C}_8 , the symmetric positive definite mass matrix \mathbf{M} can be obtained.

2.2. Stability Analysis

In this section, the stability of the system is investigated based on the Lyapunov stability criterion. The variable $\mathbf{u} = EA \Delta \mathbf{q}$ is defined, where E and A are the Young’s modulus of elasticity and cross-sectional area of the cables, respectively. Moreover, to express the equations of the flexible system in the form of the perturbed system, the variable ε is defined, based on the cable stiffness and damping, as:

$$\varepsilon^2 = \frac{1}{EA}, \quad c_d = \frac{\alpha}{\varepsilon}, \quad \alpha = O(1) \tag{9}$$

where c_d is the damping coefficient of the cable per unit length. In the presence of cable flexibility, the angular acceleration vector of CDPR motors presented in the appendix changes as follows:

$$\ddot{\boldsymbol{\beta}} = \frac{\varepsilon^2}{r_p} \ddot{\mathbf{u}} + \mathbf{C}_3 (\mathbf{C}_6 \ddot{\boldsymbol{\theta}} + \mathbf{C}_7 \dot{\varphi}_A \dot{\boldsymbol{\theta}}) + \mathbf{C}_4 (\mathbf{C}_8 \ddot{\mathbf{x}}_B + \mathbf{C}_9) + \mathbf{C}_5 \tag{10}$$

By eliminating the cable force between Eqs. (4) and (8), we have

$$\begin{aligned}
 & \mathbf{C}_8^T ([M_B] + \mathbf{C}_4^T \mathbf{I}_m \mathbf{C}_4) \mathbf{C}_8 \ddot{\mathbf{x}}_B + \mathbf{C}_8^T \mathbf{C}_4^T \mathbf{I}_m (\mathbf{C}_3 + \mathbf{C}_{10}) \mathbf{C}_6 \ddot{\boldsymbol{\theta}} + \mathbf{C}_8^T [M_B] \mathbf{C}_9 \\
 & + \mathbf{C}_8^T \mathbf{C}_4^T \mathbf{I}_m (\mathbf{C}_3 + \mathbf{C}_{10}) \mathbf{C}_7 \dot{\varphi}_A \dot{\boldsymbol{\theta}} + \mathbf{C}_8^T \mathbf{C}_4^T \mathbf{I}_m (\mathbf{C}_4 \mathbf{C}_9 + \mathbf{C}_5) + \begin{bmatrix} \mathbf{0}_{3 \times 1} \\ \mathbf{P}_B^T (\mathbf{P}_B \dot{\boldsymbol{\psi}}_B \times \mathbf{I}_B \mathbf{P}_B \dot{\boldsymbol{\psi}}_B) \end{bmatrix} \\
 & + \mathbf{C}_8^T \begin{bmatrix} \mathbf{0}_{2 \times 1} \\ -m_b g \\ \mathbf{0}_{3 \times 1} \end{bmatrix} = \mathbf{C}_8^T \mathbf{C}_4^T \left(\boldsymbol{\tau}_\beta - \frac{\varepsilon^2 \mathbf{I}_m}{r_p} \ddot{\mathbf{u}} \right)
 \end{aligned} \tag{11}$$

Repeating similar operation for Eqs. (5) and (8) one can conclude that:

$$\begin{aligned}
 & [\mathbf{I}_w + \mathbf{C}_6^T ([M_A]) \mathbf{C}_6 + \mathbf{C}_6^T (\mathbf{C}_3 + \mathbf{C}_{10})^T \mathbf{I}_m (\mathbf{C}_3 + \mathbf{C}_{10}) \mathbf{C}_6] \ddot{\boldsymbol{\theta}} + \mathbf{C}_6^T (\mathbf{C}_3^T + \mathbf{C}_{10}^T) \mathbf{I}_m \mathbf{C}_4 \mathbf{C}_8 \ddot{\mathbf{x}}_B \\
 & + \mathbf{C}_6^T (\mathbf{C}_3^T + \mathbf{C}_{10}^T) \mathbf{I}_m ((\mathbf{C}_3 + \mathbf{C}_{10}) \mathbf{C}_7 \dot{\varphi}_A \dot{\boldsymbol{\theta}} + \mathbf{C}_4 \mathbf{C}_9 + \mathbf{C}_5) + \mathbf{C}_6^T [M_A] \mathbf{C}_7 \dot{\varphi}_A \dot{\boldsymbol{\theta}} \\
 & + \mathbf{C}_6^T \begin{bmatrix} \mathbf{0}_{3 \times 1} \\ \dot{\boldsymbol{\psi}}_A \times \mathbf{I}_A \dot{\boldsymbol{\psi}}_A \end{bmatrix} = \boldsymbol{\tau}_\theta + \mathbf{C}_6^T \mathbf{C}_3^T \left(\boldsymbol{\tau}_\beta - \frac{\varepsilon^2 \mathbf{I}_m}{r_p} \ddot{\mathbf{u}} \right)
 \end{aligned} \tag{12}$$

Substituting Eq. (10) in Eq. (8), we have

$$\begin{aligned}
 & \mathbf{I}_m \left(\frac{\varepsilon^2}{r_p} \ddot{\mathbf{u}} + \mathbf{C}_3 (\mathbf{C}_6 \ddot{\boldsymbol{\theta}} + \mathbf{C}_7 \dot{\varphi}_A \dot{\boldsymbol{\theta}}) + \mathbf{C}_4 (\mathbf{C}_8 \ddot{\mathbf{x}}_B + \mathbf{C}_9) + \mathbf{C}_5 \right) + \mathbf{I}_m \mathbf{C}_{10} \mathbf{C}_6 \ddot{\boldsymbol{\theta}} + \mathbf{I}_m \mathbf{C}_{10} \mathbf{C}_7 \dot{\varphi}_A \dot{\boldsymbol{\theta}} \\
 & + r_p \text{diag}^{-1}(\mathbf{q}_u) (\mathbf{u} + c_d \varepsilon^2 \dot{\mathbf{u}}) = \boldsymbol{\tau}_\beta
 \end{aligned} \tag{13}$$

In the perturbed Eqs. (11–13), the variables \mathbf{x}_B and $\boldsymbol{\theta}$ indicate the slow dynamic of the system, whereas \mathbf{u} is the fast dynamic variable introduced by the oscillations of the viscoelastic cables. By assuming $\varepsilon = 0$ and $\Delta \mathbf{q} = \mathbf{0}$, these equations will be reduced to the rigid model equations. Ignoring second-order term ε^2 in Eq. (13) results in:

$$\mathbf{u}_0 + \alpha \varepsilon \dot{\mathbf{u}}_0 = \frac{\text{diag}(\mathbf{q}_u)}{r_p} (\boldsymbol{\tau}_{\beta_0} - \mathbf{I}_m ((\mathbf{C}_3 + \mathbf{C}_{10}) (\mathbf{C}_6 \ddot{\boldsymbol{\theta}} + \mathbf{C}_7 \dot{\varphi}_A \dot{\boldsymbol{\theta}}) + \mathbf{C}_4 (\mathbf{C}_8 \ddot{\mathbf{x}}_B + \mathbf{C}_9) + \mathbf{C}_5)) \quad (14)$$

On the other hand, employing the Tikhonov theory, the variables \mathbf{x}_B , $\boldsymbol{\theta}$, and \mathbf{u} can be approximated as follows:¹⁹

$$\begin{cases} \mathbf{u} = \mathbf{u}_0(t) + \delta(\tau) + \mathbf{O}(\varepsilon) \\ \mathbf{x}_B = \mathbf{x}_{B_0}(t) + \mathbf{O}(\varepsilon) \\ \boldsymbol{\theta} = \boldsymbol{\theta}_0(t) + \mathbf{O}(\varepsilon) \end{cases} \quad (15)$$

where $\tau = t/\varepsilon$ and δ indicate the timescale and the variable of the fast dynamic. The control effort applied to the CDPR’s motors is considered to be $\boldsymbol{\tau}_\beta = \boldsymbol{\tau}_{\beta_0} + \boldsymbol{\tau}_{\beta_\delta}$, where $\boldsymbol{\tau}_{\beta_0}$ is obtained from the rigid dynamic model and $\boldsymbol{\tau}_{\beta_\delta}$ is an auxiliary torque applied to stabilize the fast dynamic if necessary. Therefore, substituting $\boldsymbol{\tau}_{\beta_0}$ from Eq. (14) into Eq. (13) results in:

$$\frac{\mathbf{I}_m}{r_p} \frac{d^2 \delta}{d\tau^2} + r_p \text{diag}^{-1}(\mathbf{q}_u) \left(\delta + \alpha \frac{d\delta}{d\tau} \right) = \boldsymbol{\tau}_{\beta_\delta} \quad (16)$$

In the case of insufficient damping of the cables, the stability of the system can be guaranteed using $\boldsymbol{\tau}_{\beta_\delta} = -\mathbf{K}_\delta \varepsilon \dot{\mathbf{u}}$. As a result Eq. (16) can be rewritten as:

$$\frac{\mathbf{I}_m}{r_p^2} \frac{d^2 \delta}{d\tau^2} + \left(\frac{\mathbf{K}_\delta}{r_p} + \frac{\alpha}{\text{diag}(\mathbf{q}_u)} \right) \frac{d\delta}{d\tau} + \frac{1}{\text{diag}(\mathbf{q}_u)} \delta = \mathbf{0} \quad (17)$$

Equation (17) can be represented in time domain as:

$$\begin{bmatrix} \dot{\delta} \\ \ddot{\delta} \end{bmatrix} = \begin{bmatrix} \mathbf{0} & \mathbf{1} \\ -\mathbf{K}_1 & -\mathbf{K}_2 \end{bmatrix} \begin{bmatrix} \delta \\ \dot{\delta} \end{bmatrix} \quad (18)$$

where

$$\mathbf{K}_1 = \frac{r_p^2 EA}{\mathbf{I}_m \text{diag}(\mathbf{q}_u)}, \quad \mathbf{K}_2 = \frac{r_p^2 \sqrt{EA}}{\mathbf{I}_m} \left(\frac{\mathbf{K}_\delta}{r_p} + \frac{\alpha}{\text{diag}(\mathbf{q}_u)} \right)$$

In the case of insufficient damping, if the auxiliary term of the control effort is not applied, then the cables’ tension and the end-effector vibration increase. However, applying $\boldsymbol{\tau}_{\beta_\delta}$ requires the feedback of cables elongation rate or the direct feedback of the end-effector’s angular and translational velocities, in addition to the motors’ feedback. In this study, it is assumed that the proportional damping of the cables is available. Therefore, the virtual damping provided by the auxiliary term $\boldsymbol{\tau}_{\beta_\delta}$ can be ignored and the additional feedbacks are not required.

Considering rigid cable model and $\varepsilon = 0$, Eqs. (11) and (12) can be modified to express the dynamic equations of the rigid model as follows:

$$\mathbf{M} \ddot{\mathbf{x}} + \mathbf{C}(\mathbf{x}, \dot{\mathbf{x}}) + \mathbf{G} = \mathbf{F} \boldsymbol{\tau}, \quad \mathbf{x} = [\mathbf{x}_B^T \quad \boldsymbol{\theta}^T]^T, \quad \boldsymbol{\tau} = \begin{bmatrix} \boldsymbol{\tau}_{\beta_0} \\ \boldsymbol{\tau}_\theta \end{bmatrix} \quad (19)$$

where the expressions for \mathbf{M} , \mathbf{C} , \mathbf{G} , and \mathbf{F} are provided in the appendix. The input–output feedback linearization control law for the system expressed in Eq. (19) is as follows:

$$\boldsymbol{\tau} = \mathbf{F}^{-1} \left(\mathbf{M} \bar{\mathbf{S}}^{-1} \left(\mathbf{v} - \begin{bmatrix} \mathbf{0}_{6 \times 1} \\ \dot{\mathbf{S}} \dot{\boldsymbol{\theta}} \end{bmatrix} \right) + \mathbf{C} + \mathbf{G} \right) \quad (20)$$

where

$$S = \begin{bmatrix} C_6 & (1:2, 1:2) \\ & I_2 \end{bmatrix}, \quad \bar{S} = \begin{bmatrix} I_6 & 0_{6 \times 2} \\ 0_{2 \times 6} & C_6 & (1:2, 1:2) \end{bmatrix}$$

$$v = \ddot{x}_d + K_p e + K_d \dot{e}, \quad e = x_d - x, \quad x = [x_B^T \quad x_A(1:2)^T]^T$$

The desired and actual trajectories of the system are denoted by x_d and x , respectively. The matrices K_p and K_d are the proportional and derivative gains of the controller. This research assumes that the end-effector remains in its workspace defined in the frame of the wheeled mobile platform. The CDPRs' workspace has been investigated by many researchers and is not in the scope of this research. Remaining in the workspace prevents the singularity of the Jacobian matrix and also the matrix F in Eq. (20). Using Eqs. (9), (15), and (20), the dynamic equations of the end-effector and the platform, Eqs. (11) and (12), can be presented as:

$$\begin{bmatrix} \dot{e} \\ \ddot{e} \end{bmatrix} = \begin{bmatrix} 0 & I \\ -K_p & -K_d \end{bmatrix} \begin{bmatrix} e \\ \dot{e} \end{bmatrix} + \begin{bmatrix} 0 & 0 \\ C_{\delta_p} & C_{\delta_d} \end{bmatrix} \begin{bmatrix} \delta \\ \dot{\delta} \end{bmatrix} \tag{21}$$

where

$$C_{\delta_p} = r \bar{S} M^{-1} \begin{bmatrix} C_8^T C_4^T \text{diag}^{-1}(q_u) \\ C_6^T C_3^T \text{diag}^{-1}(q_u) \end{bmatrix}, \quad C_{\delta_d} = c_d C_{\delta_p}$$

Therefore, Eqs. (18) and (21) represent the dynamics of the closed loop system. In order to analyze the stability of the closed loop system, the following Lyapunov candidate is considered:

$$V = \frac{1}{2} \begin{bmatrix} \dot{e}^T \dot{e} + e^T K_p e + \kappa [\delta^T \quad \dot{\delta}^T] \begin{bmatrix} r_p^2 (EA + \sqrt{EA}\alpha) I & I_m \text{diag}(q_u) \\ I_m \text{diag}(q_u) & I_m \text{diag}(q_u) \end{bmatrix} \begin{bmatrix} \delta \\ \dot{\delta} \end{bmatrix} \end{bmatrix} \tag{22}$$

where $\kappa > 0$ is an arbitrary scalar. Since the employed control strategy of this paper is output feedback linearization, the stability of these states can be guaranteed using the selected function while the stability of the internal dynamics of the system is shown in ref. [18]. Using Eqs. (18) and (21), the time derivative of Eq. (22) is obtained as follows:

$$\begin{aligned} \dot{V} = & -\dot{e}^T K_d \dot{e} + \dot{e}^T [C_{\delta_p} \quad C_{\delta_d}] \begin{bmatrix} \delta \\ \dot{\delta} \end{bmatrix} - \kappa [\delta^T \quad \dot{\delta}^T] \begin{bmatrix} r_p^2 EA I & 0 \\ 0 & \alpha r_p^2 \sqrt{EA} I - I_m \text{diag}(q_u) \end{bmatrix} \begin{bmatrix} \delta \\ \dot{\delta} \end{bmatrix} \\ & + \frac{\kappa}{2} [\delta^T \quad \dot{\delta}^T] \begin{bmatrix} 0 & I_m \text{diag}(\dot{q}_u) \\ I_m \text{diag}(\dot{q}_u) & I_m \text{diag}(\dot{q}_u) \end{bmatrix} \begin{bmatrix} \delta \\ \dot{\delta} \end{bmatrix} \end{aligned} \tag{23}$$

The system stability can be shown by obtaining the necessary conditions to make \dot{V} negative semi-definite. To cover the mentioned target, the upper bound of the terms included in Eq. (23) should be specified. Considering the smallest eigenvalue of the positive definite matrix K_d , the upper bound of the first term is

$$-\dot{e}^T K_d \dot{e} \leq -\lambda_{\min}(K_d) \|\dot{e}\| = -\lambda_{md} \|\dot{e}\|^2 \tag{24}$$

Denoting the maximum singular value of a matrix by $\sigma_{\max}(\cdot)$, the upper bound of the second term can be obtained as:

$$\dot{e}^T [C_{\delta_p} \quad C_{\delta_d}] \begin{bmatrix} \delta \\ \dot{\delta} \end{bmatrix} \leq \|\dot{e}\| \left\| \begin{bmatrix} \delta \\ \dot{\delta} \end{bmatrix} \right\| \sigma_{\max}([C_{\delta_p} \quad C_{\delta_d}]) = \sigma_{me} \|\dot{e}\| \left\| \begin{bmatrix} \delta \\ \dot{\delta} \end{bmatrix} \right\| \tag{25}$$

Since $q_{u_i}(t) > 0, i = 1..6$ is always valid during the operation, assuming the following condition:

$$c_d > \frac{I_m}{r_p^2} \max(q_u) \tag{26}$$

gives the upper bound of the third term in Eq. (23) as below:

$$\begin{aligned}
 & -\kappa \begin{bmatrix} \delta \\ \dot{\delta} \end{bmatrix}^T \begin{bmatrix} r_p^2 EA \mathbf{I} & \mathbf{0} \\ \mathbf{0} & r_p^2 c_d \mathbf{I} - \mathbf{I}_m \text{diag}(\mathbf{q}_u) \end{bmatrix} \begin{bmatrix} \delta \\ \dot{\delta} \end{bmatrix} \\
 & \leq -\kappa \lambda_{\min} \left(\begin{bmatrix} r_p^2 EA \mathbf{I} & \mathbf{0} \\ \mathbf{0} & r_p^2 c_d \mathbf{I} - \mathbf{I}_m \text{diag}(\mathbf{q}_u) \end{bmatrix} \right) \left\| \begin{bmatrix} \delta \\ \dot{\delta} \end{bmatrix} \right\|^2 = -\kappa \lambda_{m\delta} \left\| \begin{bmatrix} \delta \\ \dot{\delta} \end{bmatrix} \right\|^2, \lambda_{m\delta} > 0 \quad (27)
 \end{aligned}$$

The vector of the cable length rate, $\dot{\mathbf{q}}_u$, depends on the CDPR motor shaft speed, $\dot{\boldsymbol{\beta}}$. Therefore, considering the maximum allowable motor speed, denoted by $\omega > 0$, the last term in Eq. (23) has the following upper bound:

$$\frac{\kappa}{2} \begin{bmatrix} \delta^T & \dot{\delta}^T \end{bmatrix} \begin{bmatrix} \mathbf{0} & \mathbf{I}_m \text{diag}(\dot{\mathbf{q}}_u) \\ \mathbf{I}_m \text{diag}(\dot{\mathbf{q}}_u) & \mathbf{I}_m \text{diag}(\dot{\mathbf{q}}_u) \end{bmatrix} \begin{bmatrix} \delta \\ \dot{\delta} \end{bmatrix} \leq \frac{\kappa}{2} \left\| \begin{bmatrix} \delta \\ \dot{\delta} \end{bmatrix} \right\|^2 \sigma_{\max} \left(\begin{bmatrix} \mathbf{0} & \mathbf{I}_m r_p \omega \\ \mathbf{I}_m r_p \omega & \mathbf{I}_m r_p \omega \end{bmatrix} \right) = \kappa \sigma_{mq} \left\| \begin{bmatrix} \delta \\ \dot{\delta} \end{bmatrix} \right\|^2 \quad (28)$$

where σ_{mq} can be obtained as follows:

$$\sigma_{mq} = 0.809 \mathbf{I}_m r_p \omega \quad (29)$$

As a result, the upper bound of \dot{V} can be obtained as follows:

$$\dot{V} \leq - \begin{bmatrix} \|\dot{\mathbf{e}}\| & \left\| \begin{bmatrix} \delta \\ \dot{\delta} \end{bmatrix} \right\| \end{bmatrix} \begin{bmatrix} \lambda_{md} & -\frac{\sigma_{me}}{2} \\ -\frac{\sigma_{me}}{2} & \kappa (\lambda_{m\delta} - \sigma_{mq}) \end{bmatrix} \begin{bmatrix} \|\dot{\mathbf{e}}\| \\ \left\| \begin{bmatrix} \delta \\ \dot{\delta} \end{bmatrix} \right\| \end{bmatrix} \quad (30)$$

In order to meet the goal $\dot{V} \leq 0$, the following conditions should be satisfied:

$$\lambda_{md} \geq \frac{\sigma_{me}^2}{4\kappa (\lambda_{m\delta} - \sigma_{mq})} \quad (31)$$

$$\lambda_{m\delta} > \sigma_{mq} \quad (32)$$

Since the arbitrary scalar κ can be chosen large enough to fulfill the conditions of Eq. (34), the derivative gain, \mathbf{K}_d , only needs to be positive definite. Using Eqs. (27) and (29), the condition (32) can be fulfilled by:

$$c_d > \frac{\mathbf{I}_m}{r_p^2} \max(\mathbf{q}_u) + 0.809 \mathbf{I}_m r_p \omega \quad (33)$$

Therefore, considering Eq. (33) the stability of the system is guaranteed. Indeed, Eq. (33) imposes a limitation on the damping property of the cables.

3. Optimal Feedback Linearization Control

The optimal control input of the nonlinear system can be found using LQR control law, when the error dynamic is linearized using feedback linearization approach. The control signal of the outer loop of the feedback linearization control law is obtained by minimizing the performance function expressed as follows:

$$J_{set} = \int_t^\infty (\mathbf{e}_{set}^T \mathbf{Q} \mathbf{e}_{set} + \mathbf{v}^T \mathbf{R} \mathbf{v}) dt, \quad \mathbf{e}_{set}^T = [\mathbf{e}^T \quad \dot{\mathbf{e}}^T] \quad (34)$$

$$\dot{\mathbf{e}}_{set} = \mathbf{A} \mathbf{e}_{set} + \mathbf{B} \mathbf{v} \quad (35)$$

The vector \mathbf{v} is the control signal of the feedback linearized system. The vector \mathbf{e}_{set} denotes the error of the end-effector pose and the platform position. The matrices \mathbf{Q} and \mathbf{R} are symmetric positive definite weight matrices of tracking error and control effort, respectively. The matrices \mathbf{A} and \mathbf{B} can be extracted as follows:

$$\mathbf{A} = \begin{bmatrix} \mathbf{0}_8 & \mathbf{I}_8 \\ \mathbf{0}_8 & \mathbf{0}_8 \end{bmatrix}, \quad \mathbf{B} = \begin{bmatrix} \mathbf{0}_8 \\ -\mathbf{I}_8 \end{bmatrix} \tag{36}$$

According to the optimal control law, the state feedback control signal $\mathbf{v} = -\mathbf{K} \mathbf{e}_{\text{set}}$ minimizes the performance function, where the state feedback gain is

$$\mathbf{K} = \mathbf{R}^{-1} \mathbf{B}^T \mathbf{P} \tag{37}$$

The positive definite matrix \mathbf{P} can be obtained by solving the following algebraic Riccati equation:

$$\mathbf{A}^T \mathbf{P} + \mathbf{P} \mathbf{A} - \mathbf{P} \mathbf{B} \mathbf{R}^{-1} \mathbf{B}^T \mathbf{P} + \mathbf{Q} = \mathbf{0} \tag{38}$$

4. Constrained Control Signal

The saturation constraint on the control effort may be destructive for the system response, since it is not considered in the control strategy. Therefore, the desired path of the platform and the end-effector should be designed in a way that the saturation does not occur or happen for a short period of time. For the cable robot control for which the control effort is tension, the control law can be obtained considering the tension bounds.^{20,21} One approach that improves the system response in this condition is the FHMPC. This controller can be used in either linear or nonlinear states. However, the nonlinear approach requires more control computation. In this paper, after linearizing the error dynamic using feedback linearization method, the optimal control signal is obtained using FHMPC, considering the saturation constraints.

The discretized representation of the feedback linearized system can be presented as:

$$\mathbf{e}_{\text{set}}(k+1) = \mathbf{A}_d \mathbf{e}_{\text{set}}(k) + \mathbf{B}_d \mathbf{v} \tag{39}$$

The performance function of the system is expressed as:

$$J_{\text{set}} = \sum_{k=0}^{N-1} ((\mathbf{e}_{\text{set}}(k))^T \mathbf{Q} \mathbf{e}_{\text{set}}(k) + \mathbf{v}^T(k) \mathbf{R} \mathbf{v}(k)) + \mathbf{e}_{\text{set}}(N)^T \mathbf{P} \mathbf{e}_{\text{set}}(N) \tag{40}$$

At each time step, the optimal control effort should be obtained over a finite future horizon of N steps. By arranging the states and the inputs into a vector form:

$$\begin{aligned} \mathbf{E} &= [\mathbf{e}_{\text{set}}(1)^T \quad \dots \quad \mathbf{e}_{\text{set}}(N)^T]^T \\ \mathbf{U} &= [\mathbf{v}(0)^T \quad \dots \quad \mathbf{v}(N-1)^T]^T \end{aligned} \tag{41}$$

Equations (39) and (40) for N horizon steps can be written as:

$$\mathbf{E}(k+1) = \bar{\mathbf{L}} \mathbf{U} + \bar{\mathbf{T}} \mathbf{e}_{\text{set}}(0) \tag{42}$$

$$J_{\text{set}} = \frac{1}{2} \mathbf{U}^T \mathbf{H} \mathbf{U} + \mathbf{e}_{\text{set}}(0)^T \mathbf{F} \mathbf{U} \tag{43}$$

where

$$\bar{\mathbf{L}} = \begin{bmatrix} \mathbf{B} & \mathbf{0} & \dots & \mathbf{0} \\ \mathbf{AB} & \mathbf{B} & \dots & \mathbf{0} \\ \vdots & \dots & \ddots & \vdots \\ \mathbf{A}^{N-1} \mathbf{B} & \mathbf{A}^{N-2} \mathbf{B} & \dots & \mathbf{B} \end{bmatrix}, \quad \bar{\mathbf{T}} = \begin{bmatrix} \mathbf{A} \\ \mathbf{A}^2 \\ \vdots \\ \mathbf{A}^N \end{bmatrix}, \quad \bar{\mathbf{Q}} = \begin{bmatrix} \mathbf{Q} & \mathbf{0} & \dots & \mathbf{0} \\ \mathbf{0} & \ddots & \vdots & \vdots \\ \vdots & \dots & \mathbf{Q} & \mathbf{0} \\ \mathbf{0} & \dots & \mathbf{0} & \mathbf{P} \end{bmatrix}_{N \times N}, \quad \bar{\mathbf{R}} = \begin{bmatrix} \mathbf{R} & \mathbf{0} & \dots & \mathbf{0} \\ \mathbf{0} & \ddots & \vdots & \vdots \\ \vdots & \dots & \ddots & \mathbf{0} \\ \mathbf{0} & \dots & \mathbf{0} & \mathbf{R} \end{bmatrix}_{N \times N}$$

$$\mathbf{F} = 2 \bar{\mathbf{T}}^T \bar{\mathbf{Q}} \bar{\mathbf{L}}, \quad \mathbf{H} = 2 (\bar{\mathbf{R}} + \bar{\mathbf{L}}^T \bar{\mathbf{Q}} \bar{\mathbf{L}})$$

Considering the relation between the torque and voltage in permanent DC motors which is:

$$\mathbf{v} = \mathbf{K}_1 \boldsymbol{\tau} + \mathbf{K}_2 \begin{bmatrix} \dot{\boldsymbol{\beta}} \\ \dot{\boldsymbol{\theta}} \end{bmatrix} \tag{44}$$

the control law in Eq. (20) can be rewritten as:

$$\mathbf{v} = \mathbf{K}_1 \mathbf{F}^{-1} \left(\mathbf{M} \bar{\mathbf{S}}^{-1} \left(\mathbf{v} - \begin{bmatrix} \mathbf{0}_{6 \times 1} \\ \dot{\mathbf{S}} \dot{\boldsymbol{\theta}} \end{bmatrix} \right) + \mathbf{C} + \mathbf{G} \right) + \mathbf{K}_2 \begin{bmatrix} \dot{\boldsymbol{\theta}} \\ \dot{\boldsymbol{\theta}} \end{bmatrix} \quad (45)$$

$$\mathbf{v}_{\min} < \mathbf{v} < \mathbf{v}_{\max}$$

\mathbf{v}_{\min} and \mathbf{v}_{\max} are the minimum and maximum values of the control effort. If in Eq. (45) the electrical constant matrices of \mathbf{K}_1 and \mathbf{K}_2 would be set equal to identity and zero matrices, respectively, the control voltage of the motors will be replaced by the input control torques. In addition, if the equivalent moment of inertia of the motors would be considered to be zero, then the control torque can be calculated for the output shaft of the motors.

The optimal control signal of the linearized feedback system is calculated using the performance function at each time step. Therefore, the bound of the motors' control effort should be transformed into the constraints for the feedback linearized system. Using Eq. (45), the saturation constraint can be expressed as:

$$\mathbf{A}_v \mathbf{v} \leq \mathbf{B}_v \quad (46)$$

where

$$\begin{aligned} \mathbf{A}_v(\mathbf{i}, \mathbf{j}) &= \bar{\mathbf{A}}_v, \quad \mathbf{B}_v(\mathbf{i}, 1) = \bar{\mathbf{B}}_v \\ \mathbf{i} &= 16k + 1 : 16(K + 1) \\ \mathbf{j} &= 8k + 1 : 8(K + 1), \quad k = 0 : H_n - 1 \\ \bar{\mathbf{A}}_v &= \begin{bmatrix} \bar{\mathbf{a}}_v \\ -\bar{\mathbf{a}}_v \end{bmatrix}, \quad \bar{\mathbf{B}}_v = \begin{bmatrix} \bar{\mathbf{b}}_v \\ -\bar{\mathbf{b}}_v \end{bmatrix} + \begin{bmatrix} \mathbf{v}_{\max} \\ -\mathbf{v}_{\min} \end{bmatrix} \\ \bar{\mathbf{a}}_v &= \mathbf{K}_1 \mathbf{F}^{-1} \mathbf{M} \bar{\mathbf{S}}^{-1} \\ \bar{\mathbf{b}}_v &= \mathbf{K}_1 \mathbf{F}^{-1} \left(\mathbf{M} \bar{\mathbf{S}}^{-1} \begin{bmatrix} \mathbf{0}_{6 \times 1} \\ \dot{\mathbf{S}} \dot{\boldsymbol{\theta}} \end{bmatrix} - (\mathbf{C} + \mathbf{G}) \right) - \mathbf{K}_2 \begin{bmatrix} \dot{\boldsymbol{\theta}} \\ \dot{\boldsymbol{\theta}} \end{bmatrix} \end{aligned}$$

Overall scheme of the proposed controller can be seen as the following block diagram. As can be seen, the optimal control is first calculated according to the predefined strategy of LQR or FHMPC. Then, the final control input extracted from the saturation filter is applied to the robot plant. The block diagram of the proposed controlling strategy is shown in Figure 2.

5. Simulation

In this section, the results of two simulations are shown. First, the optimal control of the wheeled mobile CDPR is carried out using LQR and FHMPC. The saturation constraints are incorporated during the simulation. Afterwards, the effect of cable sag is considered in the direct dynamic simulation and the results are compared with the case for which the sagging is not incorporated.

5.1. Trajectory tracking using optimal feedback linearization control

The end points of the cables are located on the triangular end-effector and the platform. The geometrical parameters of the robot are provided in Table I. The cables' stiffness and damping are considered $EA = 15000$ N and $cd = 1$ N.s/m². The desired path of the platform and the end-effector are considered as a circular curve which is within the workspace of the robot:

$$\mathbf{x}_A = \begin{bmatrix} R \sin(\varphi) \\ -R \cos(\varphi) \\ \mathbf{0}_{3 \times 1} \\ \varphi \end{bmatrix}, \quad \mathbf{x}_B = \begin{bmatrix} \mathbf{x}_{A_{1,2}} \\ 0.8 + 0.1 \sin\left(\frac{\pi}{7}t\right) \\ \mathbf{x}_{A_{4,6}} \end{bmatrix} \quad (47)$$

where

$$\varphi = \frac{-4\omega_p}{(3T^2)} \left(t - \frac{T}{2} \right)^3 + \omega_p t - \frac{\pi}{2}, \quad \omega_p = \frac{3\pi}{T}, \quad T = 10, \quad R = 1.5$$

Table I. Geometrical parameters.

Name	Symbol	Value	Unit
Side length of the triangular upper plate of the platform	–	1.19	m
Side length of the triangular end-effector	–	0.17	m
Distance between Z axis of the platform and the line connecting the driving wheels	d	0.31	m
Half of the distance between the wheels	b	0.54	m
Radius of the driving wheels	r_{wh}	0.1	m
Radius of the cable drums	r	0.015	m

Table II. Dynamical parameters.

Name	Symbol	Value	Unit
Platform mass		170	kg
End-effector mass		1.1	kg
Moment of inertia tensor of the platform			kg.m ²
Moment of inertia tensor of the end-effector			kg.m ²
Equivalent moment of inertia of the platform motors		0.005 I_2	kg.m ²
Equivalent moment of inertia of the CDPR motors		0.0003 I_6	kg.m ²
Stall torque of the platform motors		45.17	N.m
Stall torque of the CDPR motors		2.074	N.m
No load speed of the platform motors		102	Rpm
No load speed of the CDPR motors		250	Rpm

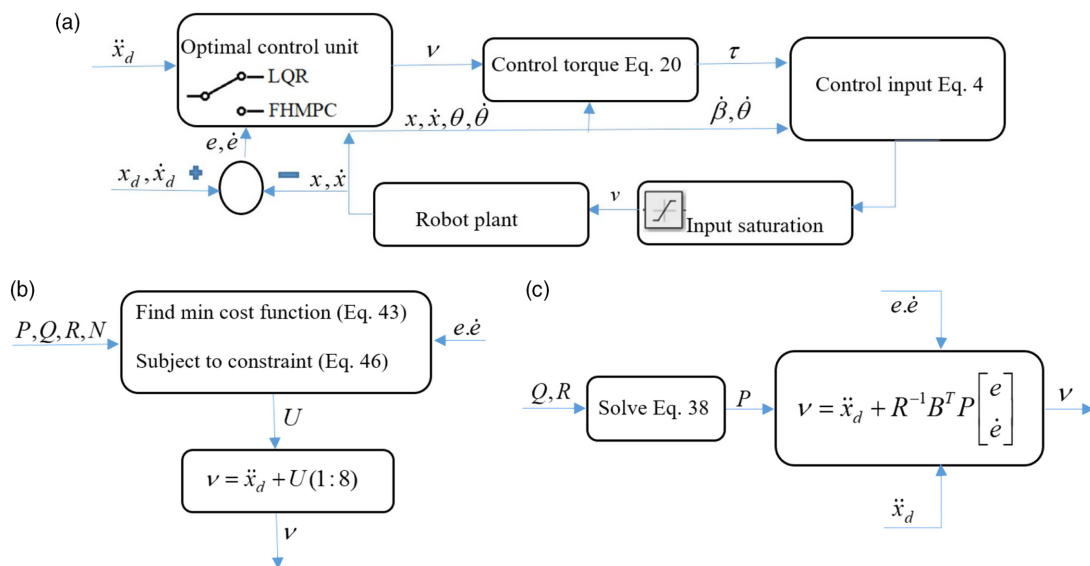


Fig. 2. (a) Block diagram of the proposed control strategy, (b) FHMPC approach, (c) LQR approach.

The weight matrices of the two optimal controllers are as follows:

$$Q = \begin{bmatrix} Q_p & 0_8 \\ 0_8 & Q_d \end{bmatrix}, \quad P = \begin{bmatrix} 200I_8 & 0_8 \\ 0_8 & 2 \text{ sqrt}(200)I_8 \end{bmatrix}, \quad R = I_8 \quad (48)$$

where

$$Q_p = 1562500 \text{ diag} (1_{2 \times 1}, 10, 1_{5 \times 1}), \quad Q_d = 16 \text{ sqrt} (Q_p)$$

The number of steps for optimal computations in FHMPC is $N = 20$ and the time step is considered to be $T = 0.00045$ s. The rest of the parameters are provided in Table II.

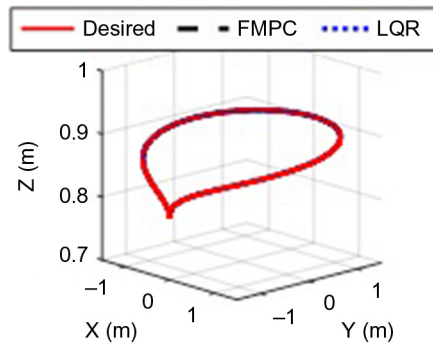


Fig. 3. Trajectory tracking of the end-effector.

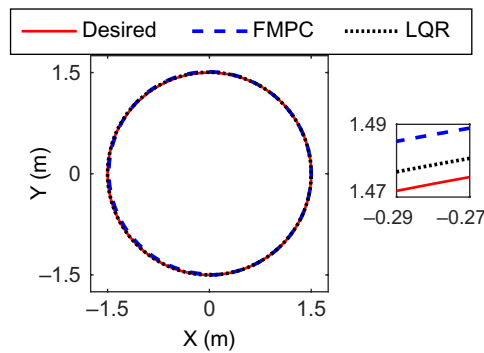


Fig. 4. Trajectory tracking of the platform.

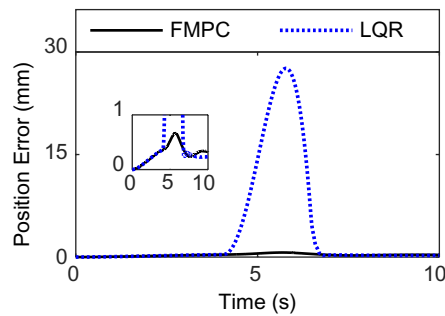


Fig. 5. The end-effector position error.

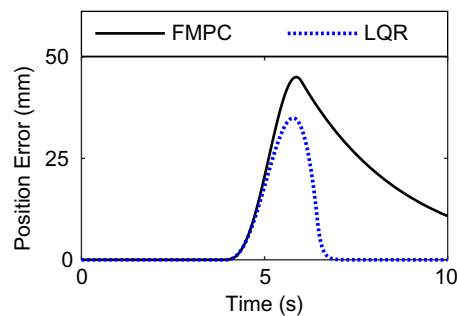


Fig. 6. The platform position error.

Figures 3 and 4 show the trajectory tracking of the platform and the end-effector. The position errors are also shown in Figs. 5 and 6. The related parameters and gains of the designed controllers are determined manually using trial and error. To obtain the parameters in this manner, the criteria such as the tracking error, settling time, and overshoot can be evaluated.

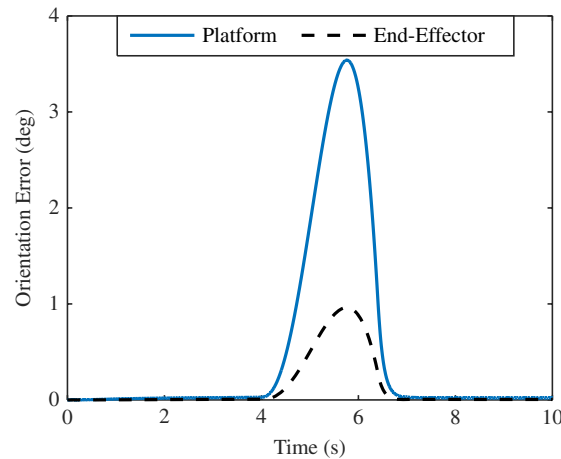


Fig. 7. The platform and end-effector orientation error.

According to the desired path equation, the velocity of the platform and the end-effector in the XY plane are parabolic with zero value at the start and end points. Similarly, the position errors have parabolic trend. The position error of the end-effector increases from zero at the beginning of the tracking to its peak value of 0.5 mm for the FHMPC and 27.5 mm for the LQR method. Afterward, both of the approaches demonstrate a decrease to below 0.5 mm at the end of the tracking. The position error of the platform with FHMPC, at the peak point and also the end of the simulation, is about 10 mm more than the error obtained by LQR. It should be noted that due to the finite and infinite horizon definitions of the performance function in Eqs. (34) and (40), similar weight matrices for the two optimal controllers cannot lead to a similar results. In other words, in order to realize a more efficient error reduction using FHMPC compared to LQR method, higher values of weight matrices are required. In this simulation, the initial weight matrices used for the FHMPC are the same as those used for the LQR. Therefore, the speed of the convergence is slower with FHMPC, and due to simulation time limit, the FHMPC has not enough time to reach to the same final position error as LQR. However, considering the large distance tracked by the platform, 10 mm position error of the platform is negligible.

Figure 7 shows that the orientational error of the end-effector and platform are not remarkable and equal roughly by the two mentioned controllers. It can be seen that the error of the rotational movement of the platform is more than the end-effector, that is, 3.5° for the platform compared to 1° for the end-effector.

In Figs. 8 and 9, the control efforts of the motors are shown. Since the movement of the left wheel is through a bigger circle, the left wheel needs higher torque, leading to the saturation of the left wheel motor in the middle of the path. Therefore, the platform deviates from the desired set point at the end of the simulation. According to the dynamic equations, the states of the chassis and cable robot are extremely coupled. Using the employed controller, the error dynamics can almost be decoupled with some perturbations resulted from the cable flexibility. Due to the actuator saturation, the platform error can affect the end-effector error. However, comparing Figs. (5) and (6) shows that the CDPR control input compensates the errors caused by the platform to some extent, as the end-effector error is smaller than the platform error, particularly using FHMPC method. From the mid-time of the simulation, the decreasing trend of the platform acceleration according to Eq. (47) results in the wheels torques reduction. In the LQR controller, this phenomenon is more impulsive, particularly when the voltage of the left wheel motor starts to decrease. As shown in Fig. 10, this abrupt shock contributes to the cable tension oscillation due to the cables elasticity, while the cable tension with FHMPC controller experiences smoother changes.

Also it can be concluded that for the end-effector in which no saturation is occurred, LQR provides more optimized control effort while for the platform actuators, FHMPC controls the system using smoother trend of control effort which shows that the proposed controller of FHMPC is more efficient for saturation conditions.

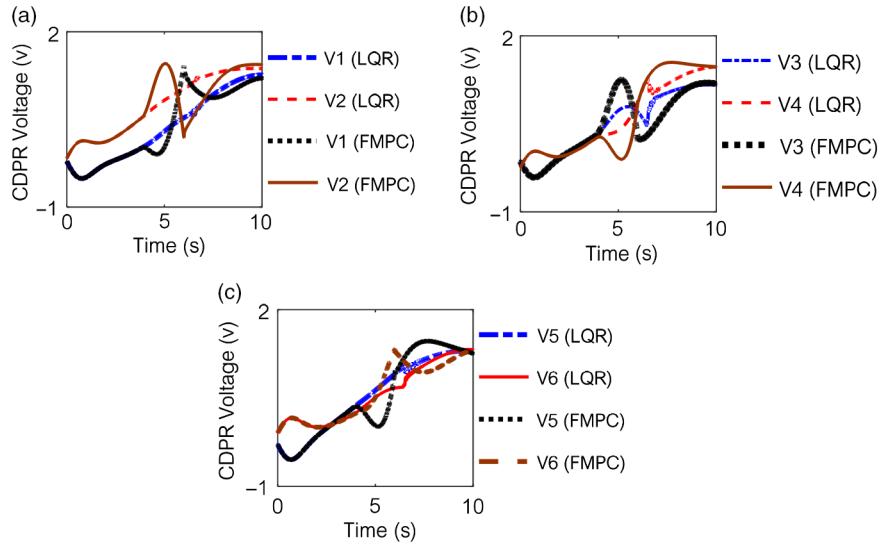


Fig. 8. (a) The first and second control signal of the CDRP, (b) the third and fourth control signal of the CDRP, and (c) the fifth and sixth control signal of the CDRP.

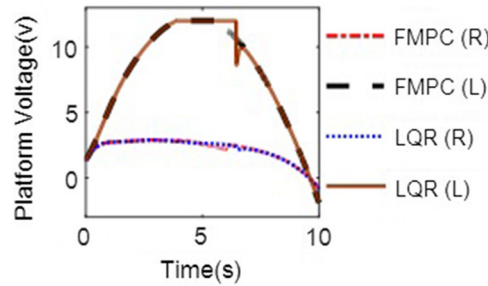


Fig. 9. The wheels control signals.

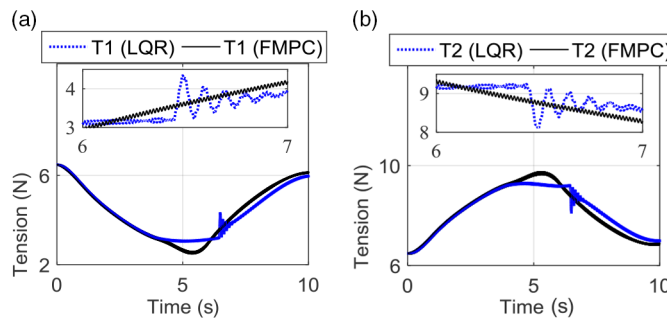


Fig. 10. (a) Tension of the first cable, (b) tension of the second cable.

5.2. Trajectory tracking considering cable sagging

Cable elasticity causes oscillation in the cable tension which leads to the end-effector vibration. Nevertheless, the damping properties of the cables reduce the end-effector vibration magnitude. The cable mass results in cable sagging. By increasing the cable robot dimensions or the robot workspace, the cable length is also increased and the effect of sagging exacerbates. In addition, the cable flexibility has direct relation with the cable length. Therefore, both, the flexibility and sagging, cause tracking error.

The cable robot used in this paper is similar in size with some of the industrial WMRs with serial link manipulator. Therefore, its cables length is shorter, in comparison with the usual CDPRs of the same workspace, used for object handling. This is one of the advantageous of the proposed robot configuration, that is, combination of a WMR with a CDPR.

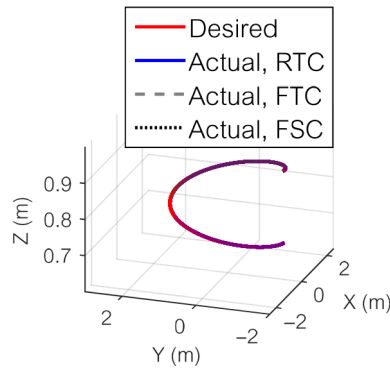


Fig. 11. Trajectory tracking of the end-effector.

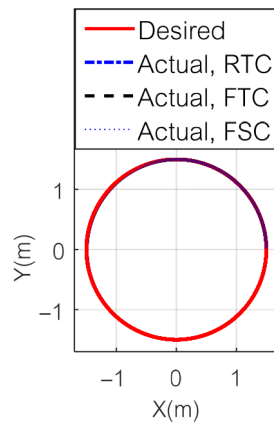


Fig. 12. Trajectory tracking of the platform.

The second simulation is performed in order to quantitatively compare the significance of the two mentioned effects, that is, cable sagging and elasticity. The curve of the cables due to the sagging is considered to be in the vertical plane. The cable tension terms in the direct dynamic equations are modified by considering quasi-static motion, while the control law remains unchanged. According to the modification process shown in ref. [22], the cable tensions on the motor side are different from the end-effector side. Therefore, Eqs. (4)–(6) should be modified for the direct dynamic simulation. The simulation is performed for the following desired path of the platform and the end-effector:

$$\begin{cases} \mathbf{x}_A = [R \sin(\varphi) \ -R \cos(\varphi) \ \mathbf{0}_{1 \times 3} \ \varphi]^T \\ \mathbf{x}_B = [\mathbf{x}_{A1} \ \mathbf{x}_{A2} + .05 \mathbf{x}_{A1} \ 0.8 + 0.1 \cos(\frac{\pi}{7}t) \ \mathbf{x}_{A4,6}^T]^T \end{cases} \quad (49)$$

where

$$\begin{aligned} \varphi &= \frac{-4\omega_p}{(3T^2)} \left(t - \frac{T}{2}\right)^3 + \omega_p t - \frac{\pi}{2} \\ \omega_p &= \frac{3\pi}{T}, \quad T = 10, \quad R = 1.5 \end{aligned}$$

According to Eq. (49), the desired velocities of the end-effector and the platform are zero at the beginning and the end of the simulation. In this simulation, feedback linearization control law is employed. The control gains are as follows:

$$\mathbf{K}_p = \text{Diag}(7.5_{2 \times 1}, 150, 7.5_{5 \times 1}), \quad \mathbf{K}_d = 2 \text{sqrt}(\mathbf{K}_p) \quad (50)$$

The rest of the parameters are shown in Tables I and II. The results of three models of the cable consisting of rigid taut cable, flexible taut cable, and flexible sagged cable are compared. Figures 11 and 12 demonstrate tracking of the end-effector and the platform, in which no considerable differences can be seen between these three cases. In these figures, RTC indicates the rigid taut cable

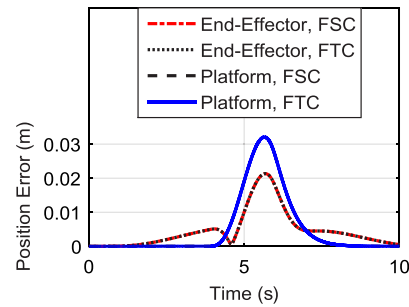


Fig. 13. Position error of the end-effector.

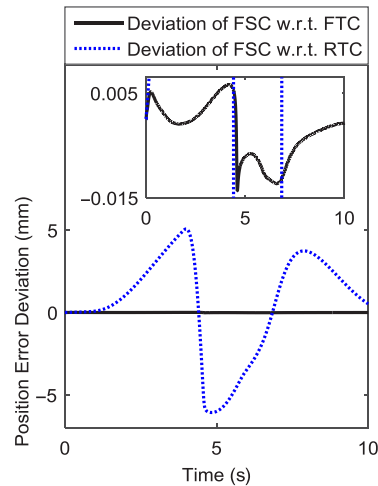


Fig. 14. Position error deviation of the end-effector.

model, FSC is flexible sagged cable model, and FTC is flexible taut cable model. Figure 13 shows that the position errors are not noticeably affected by the cable sag, as the taut cable or sag cable does not change the end-effector and platform position error. These errors are similar but different from the rigid case. This can also be observed in Fig. 14, which shows the position error difference between the flexible sagged case and the other two cases. It is shown that the maximum value of the error difference with the flexible taut case is 5 mm, while for the rigid case this error is decreased to 0.015 mm.

Based on these results, it can be concluded that for the dimension of the proposed robot, the cable elasticity has more effect on deviation of the end-effector tracking, in comparison with the cable sagging. Figure 15(a)–(f) shows the control signals of the CDPR's motors. According to Eq. (49), the end-effector moves in a spiral path while its plane is horizontal. Therefore, considering the proximity of each two cables, according to Fig. 15(a)–(f), the voltage of the associated cables is similar to each other. Furthermore, a small difference between the results of the rigid case compared to the others is visible, while the difference between the results of the FTC and FSC is not noticeable. This shows that the impact of the cable elasticity in the end-effector deviation is more severe than the cable sagging.

6. Experimental Results

In order to verify the simulation results, a robot with the mentioned structure is manufactured at the Iran University of Science and Technology called ICaSbot and can be seen in Fig. 17. The robot has two independent fixed rear wheels and one idle front caster wheel. The wheels are driven by permanent magnet DC (PMDC) motors. The cables of the CDPR part of the robot are also driven by PMDC motors. The position feedback of the platform and the end-effector are provided using the incremental encoders installed on the motor output shaft and employing the direct kinematics of

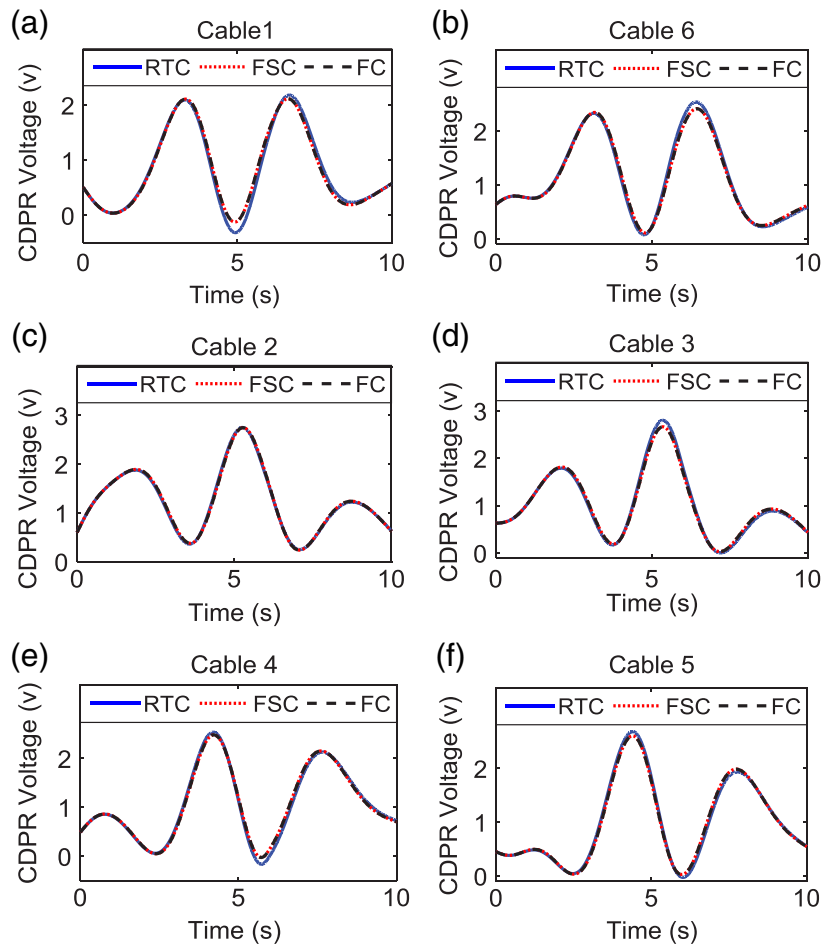


Fig. 15. (a) Voltage of the first motor, (b) voltage of the sixth motor, (c) voltage of the second motor, (d) voltage of the third motor, (e) voltage of the fourth motor, and (f) voltage of the fifth motor.

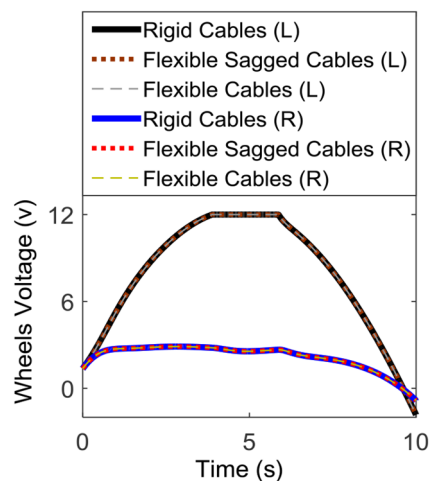


Fig. 16. Voltage of the wheels motors: right motor (R), left motor (L).

the robot. The accuracy of the end-effector pose measurement depends on the end-effector position and orientation with respect to the platform frame.

The control signals are implemented using MATLAB, where the calculated control efforts are converted to the voltage signals. These signals are then applied to the motors through some PIC microcontrollers and motor drivers.

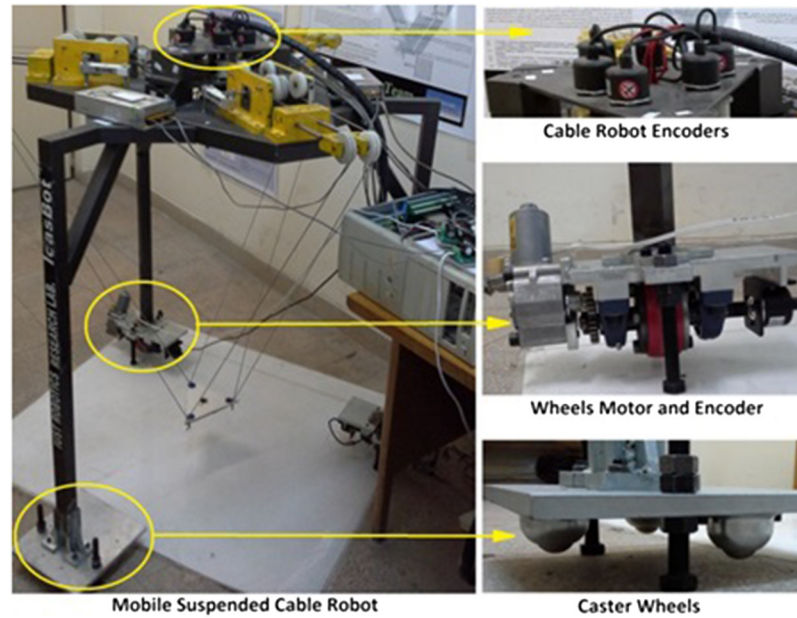


Fig. 17. ICaSbot manufactured in IUST.

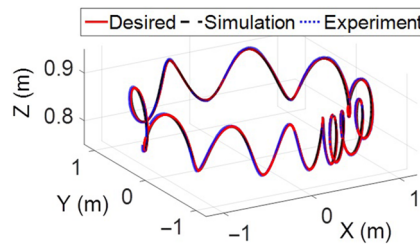


Fig. 18. Trajectory tracking of the end-effector.

The test is performed considering the desired path of the platform and the end-effector as follows:

$$\begin{cases} \mathbf{x}_A = [[\tilde{\mathbf{x}}_a(1) \quad \tilde{\mathbf{x}}_a(2) \quad 0] + \mathbf{d}_v^T \quad \mathbf{0}_{1 \times 2} \quad \tilde{\mathbf{x}}_a(6)]^T \\ \mathbf{x}_B = \mathbf{x}_A + {}^N\mathbf{R}_A [0 \quad 0.07\sin(\frac{24\pi}{T}t) \quad 0.85 + 0.05\cos(\frac{24\pi}{T}t) \quad \mathbf{0}_{1 \times 3}]^T \end{cases} \quad (51)$$

where

$$\tilde{\mathbf{x}}_A = [R \sin(\varphi) \quad -R \cos(\varphi) \quad \mathbf{0}_{1 \times 3} \quad \varphi]^T, \quad \mathbf{d}_v = d [\cos(\varphi) \quad \sin(\varphi) \quad 0]^T, \quad \varphi = \frac{-4\omega_p}{3T^2} (t - \frac{T}{2})^3 + \omega_p t - \frac{\pi}{2}$$

$$T = 125, \quad \omega_p = \frac{3\pi}{T}, \quad R = 1.08$$

$${}^N\mathbf{R}_A = \begin{bmatrix} \cos(\varphi) & -\sin(\varphi) & 0 \\ \sin(\varphi) & \cos(\varphi) & 0 \\ 0 & 0 & 1 \end{bmatrix}$$

Figures 18 and 19 demonstrate the tracking results of the platform and end-effector in simulation and experiment. It is shown that the overall motions resulted from experimental tests match the simulation. As shown in Fig. 20, the maximum position error of the experiment is about 0.025 which is only 0.015 m more than the results obtained by simulation. The maximum position error is almost equivalent to the platform maximum error in Fig. 21. The orientation error of the end-effector, measured by the 2-norm of the Euler angles, is shown in Fig. 22. It is shown that the maximum orientation error throughout the test is only 2.5°.

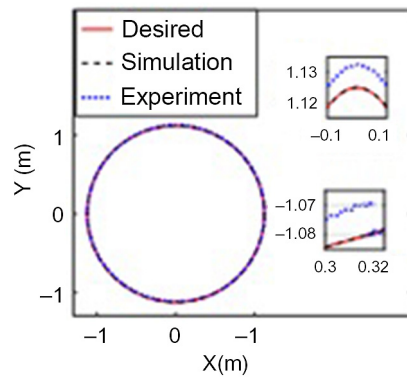


Fig. 19. Trajectory tracking of the platform.

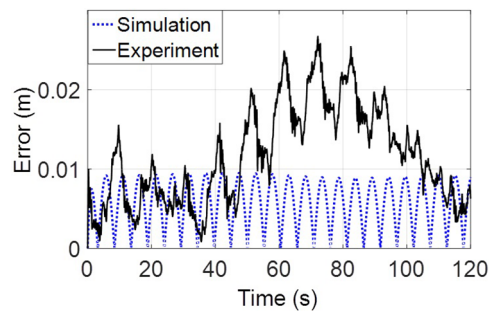


Fig. 20. End-Effector position error.

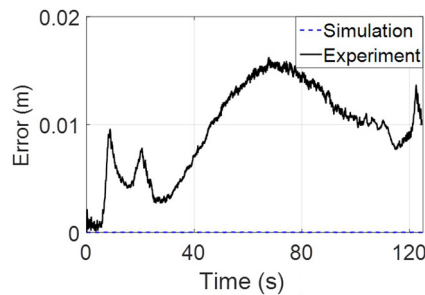


Fig. 21. Platform position error.

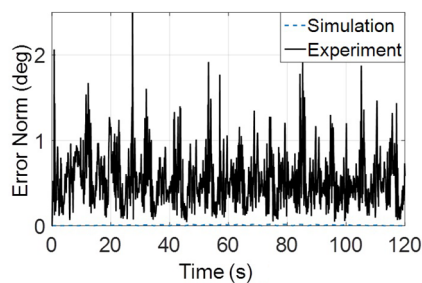


Fig. 22. Norm of the end-effector Euler angle errors.

Two sources of the mentioned errors in the system are related to the control loop delay and limitation in applying the Pulse Width Modulation (PWM). The delay time is about 30 ms, which is mainly due to the communication delay of serial protocol between the computer and microcontrollers. The same delay contributed to the sensors also can affect the results of experimental tests. On the other

hand, the internal friction in the motors limits the minimum required PWM signal. Therefore, any control signal below the minimum PWM may not result in a rotation of the motor. In addition to the Coulomb friction, a part of the internal friction also depends on the motor speed. In this paper, the frictions are ignored in the modeling.

Other parametric uncertainties in experimental setup, such as the motor backlash and alignment of the platform legs increase the error of experimental results compared with simulations. Furthermore, in order to protect the motors, the upper bound of the PWM is restricted. The limitation bounds of the eight motors considered in this test are as follows:

$$\begin{aligned} \mathbf{PWM}_{\min} &= [25_{1 \times 6} \quad 10_{1 \times 2}]^T \\ \mathbf{PWM}_{\max} &= 80_{8 \times 1} \end{aligned} \quad (52)$$

Also the motor torques in order to realize the end-effector movement are shown in Figs. D.5, D.6, D.7, and D.8.

7. Conclusion

A new cable-driven robot is proposed and modeled which is able to move using a mobile chassis. Optimal control is employed and implemented in the presence of cable viscoelasticity using LQR, whereas the control effort is bounded using FHMPC approach. In order to minimize the destructive effect of structural flexibility by reducing the cable length, a hybrid model comprising a WMR and a CDPR is proposed. The stability of the system is proven using Lyapunov stability criterion with a rigid model-based controller. It is shown that in the presence of a specified minimum damping in the cables and without using additional feedback of the cables tension rate or the end-effector pose, the system stability can be achieved using the proposed controller. The correctness of modeling and efficiency of the controller are investigated by some simulation scenarios. In the first simulation, path tracking of the robot is performed using LQR and FHMPC, where the final position error of the end-effector is below 0.5 mm for both controllers. The second simulation is conducted in order to compare the impact of cable elasticity and sag on the tracking error of the intended robot. Therefore, in the direct dynamic simulation, the cable tensions are modified. It is shown that the deviation of the position error in the case of flexible sagged cable model with respect to the rigid taut cable model is about 5 mm, whereas with respect to the flexible taut cable model is below 0.015 mm. It is demonstrated that for the proposed robot, the negative impact of the cable flexibility is more severe compared with the cable sag. Eventually, the results are verified by conducting some experimental tests on mobile cable robot of ICaSbot. It is shown that the deviation of the platform and the end-effector translational error in the test with respect to the simulation are only 1.5 cm, whereas the rotational error is just 2.5°. Considering the distance tracked by the platform, the errors are negligible and it can be concluded that the proposed robot using the designed controller can perform the payload tracking task with a good accuracy in the presence of cables elasticity in a vast workspace.

References

1. M. H. Korayem and A. M. Shafei, "A new approach for dynamic modeling of n-viscoelastic-link robotic manipulators mounted on a mobile base," *Nonlinear Dyn.* **79**(4), 2767–2786 (2015). doi: [10.1007/s11071-014-1845-8](https://doi.org/10.1007/s11071-014-1845-8)
2. M. H. Korayem, R. A. Esfeden and S. R. Nekoo, "Path planning algorithm in wheeled mobile manipulators based on motion of arms," *J. Mech. Sci. Technol.* **29**(4), 1753–1763 (2015). doi: [10.1007/s12206-015-0349-x](https://doi.org/10.1007/s12206-015-0349-x)
3. T. Fujita and H. Sugawara, "Development of a Parallel Link Arm for Object Handling by Wheeled Mobile Robot," *2014 11th International Conference on Informatics in Control, Automation and Robotics (ICINCO)*, Vienna, Austria, vol. 2 (2014) pp. 592–598. doi: [10.5220/0005116905920598](https://doi.org/10.5220/0005116905920598)
4. S. A. A. Moosavian, A. Pourreza and K. Alipour, "Dynamics and stability of a hybrid serial-parallel mobile robot," *Math. Comput. Modell. Dyn. Syst.* **16**(1), 35–56 (2010). doi: [10.1080/13873951003676518](https://doi.org/10.1080/13873951003676518)
5. Z. H. Liu, X. I. Tang and L. Wang, "Research on the dynamic coupling of the rigid-flexible manipulator," *Rob. Comput. Integr. Manuf.* **32**, 72–82 (2015). doi: [10.1016/j.rcim.2014.10.001](https://doi.org/10.1016/j.rcim.2014.10.001)
6. J. C. Santos, A. Chemori and M. Gouttefarde, "Model Predictive Control of Large-Dimension Cable-Driven Parallel Robots," *In: International Conference on Cable-Driven Parallel Robots* (Springer, Cham, 2019) pp. 221–232.

7. S. Hwang, J. Bak, J. Yoon and J. Park, "Oscillation reduction and frequency analysis of under-constrained cable-driven parallel robot with three cables," *Robotica*, 1–21 (2019). doi: [10.1017/S0263574719000687](https://doi.org/10.1017/S0263574719000687)
8. X. Diao and O. Ma, "Vibration analysis of cable-driven parallel manipulators," *Multibody Sys. Dyn.* **21**(4), 347–360 (2009). doi: [10.1007/s11044-008-9144-0](https://doi.org/10.1007/s11044-008-9144-0)
9. W. J. Shiang, D. Cannon and J. Gorman, "Dynamic Analysis of the Cable Array Robotic Crane," *IEEE International Conference Robotics and Automation*, Detroit, MI, USA, vol. 4 (1999) pp. 2495–2500. doi: [10.1109/ROBOT.1999.773972](https://doi.org/10.1109/ROBOT.1999.773972)
10. Y. Zhang, S. K. Agrawal and M. J. Piovoso, "Coupled Dynamics of Flexible Cables and Rigid End-Effector for a Cable Suspended Robot," American Control Conference, Minneapolis, MN, USA (2006) pp. 3880–3885. doi: [10.1109/ACC.2006.1657324](https://doi.org/10.1109/ACC.2006.1657324)
11. E. Laroche, R. Chellal, L. Cu villon and J. Gangloff, "A preliminary study for H-inf control of parallel cable-driven manipulators," Cable-Driven Parallel Robots, *Mech. Mach. Sci.* **12**, 353–369 (2013). doi: [10.1007/978-3-642-31988-4_22](https://doi.org/10.1007/978-3-642-31988-4_22)
12. M. A. Khosravi and H. D. Taghirad, "Dynamic analysis and control of cable driven robots with elastic cables," *Trans. Can. Soc. for Mech. Eng.* **35**(4), 543–558 (2011).
13. M. H. Korayem, H. Tourajizadeh, M. Taherifar and A. H. Korayem, "Optimal feedback linearization control of a flexible cable robot," *Lat. Am. Appl. Res.* **44**(3), 259–265 (2014).
14. M. H. Korayem, M. Taherifar and H. Tourajizadeh, "Compensating the flexibility uncertainties of a cable suspended robot using SMC approach," *Robotica* **33**(3), 578–598 (2015). doi: [10.1017/S0263574714000472](https://doi.org/10.1017/S0263574714000472)
15. R. Bostelman, J. Albus, N. Dagalakis, A. Jacoff and J. Gross, "Applications of the NIST RoboCrane," *Proceedings 5th International Symposium on Robotics and Manufacturing*, Maui, Hawaii (1994) pp. 14–18.
16. S. R. Oh, J. C. Ryu and S. K. Agrawal, "Dynamics and control of a helicopter carrying a payload using a cable-suspended robot," *J. Mech. Des.* **125**(5), 1113–1121 (2006). doi: [10.1115/1.2218882](https://doi.org/10.1115/1.2218882)
17. S. R. Oh, K. K. Mankala, S. K. Agrawal and J. S. Albus, "Dynamic modeling and robust controller design of a two-stage parallel cable robot," *Multibody Sys. Dyn.* **13**(4), 385–399 (2005). doi: [10.1007/s11044-005-2517-8](https://doi.org/10.1007/s11044-005-2517-8)
18. Y. Yamamoto and X. Yun, "Coordinating Locomotion and Manipulation of a Mobile Manipulator," *Proceedings of the 31st IEEE Conference on Decision and Control*, Tucson, AZ, USA (1992) pp. 2643–2648.
19. P. Kokotovic, H. K. Khalil and J. O'Reilly, *Singular Perturbation Methods in Control: Analysis and Design*, vol. 25 (Siam Academic Press, London, 1999).
20. H. R. Fahham, M. Farid and M. Khooran, "Time optimal trajectory tracking of redundant planar cable-suspended robots considering both tension and velocity constraints," *ASME J. Dyn. Syst.-T* **133**(1), 011004 (2011). doi: [10.1016/j.fincl.2010.10.005](https://doi.org/10.1016/j.fincl.2010.10.005)
21. E. Barnett and C. Gosselin, "Time-optimal trajectory planning of cable-driven parallel mechanisms for fully specified paths with G1-discontinuities," *ASME J. Dyn. Syst.-T* **137**(7), 071007 (2015). doi: [10.1115/1.4029769](https://doi.org/10.1115/1.4029769)
22. H. T. Thai and S. E. Kim, "Nonlinear static and dynamic analysis of cable structures," *Finite Elem. Anal. Des.* **47**(3), 237–246 (2011). doi: [10.1016/j.fincl.2010.10.005](https://doi.org/10.1016/j.fincl.2010.10.005)

Appendix

A. Coefficient Matrices of the Kinematic Equations

The acceleration vector of the platform, obtained by the derivative of Eq. (1), can be expressed as follows:

$$\ddot{\mathbf{x}}_A = \mathbf{C}_6 \ddot{\boldsymbol{\theta}} + \mathbf{C}_7 \dot{\varphi}_A \dot{\boldsymbol{\theta}} \quad (\text{A.1})$$

The end-effector acceleration vector obtained by the derivative of Eq. (2) is as follows:

$$\ddot{\mathbf{x}}_B = \mathbf{C}_8 \ddot{\mathbf{x}}_B + \mathbf{C}_9 \quad (\text{A.2})$$

The angular acceleration vector of the CDPR motors obtained considering Eq. (3) is

$$\ddot{\boldsymbol{\beta}} = \mathbf{C}_3 \ddot{\mathbf{x}}_A + \mathbf{C}_4 \ddot{\mathbf{x}}_B + \mathbf{C}_5 \quad (\text{A.3})$$

The coefficient matrices used in the kinematic equations can be defined as follows:

$$\mathbf{C}_1 = \begin{bmatrix} -{}^N\mathbf{R}_A^T & {}^A\bar{\mathbf{X}}_{BA} \\ \mathbf{0}_3 & -{}^N\mathbf{R}_B^T {}^N\mathbf{R}_A \end{bmatrix}, \quad \mathbf{C}_2 = \begin{bmatrix} {}^N\mathbf{R}_A^T & \mathbf{0}_3 \\ \mathbf{0}_3 & \mathbf{I}_3 \end{bmatrix}, \quad \mathbf{C}_3 = \frac{1}{r} \boldsymbol{\Lambda}^T \begin{bmatrix} -{}^N\mathbf{R}_A^T & {}^A\bar{\mathbf{X}}_{BA} \\ \mathbf{0}_3 & -\mathbf{I}_3 \end{bmatrix}, \quad \mathbf{C}_4 = \frac{1}{r} \boldsymbol{\Lambda}^T {}^A\bar{\mathbf{R}}_B \mathbf{C}_2 \quad (\text{A.4})$$

$$\begin{aligned}
 \mathbf{C}_5 &= \frac{1}{r} \mathbf{\Lambda}^T \begin{bmatrix} -{}^A\bar{\mathbf{W}}_{AN} {}^2N\mathbf{R}_A^T ({}^N\mathbf{x}_{BN} - {}^N\mathbf{x}_{AN}) & -{}^A\bar{\mathbf{W}}_{AN} ({}^N\mathbf{R}_A^T ({}^N\dot{\mathbf{x}}_B - {}^N\dot{\mathbf{x}}_A) + {}^A\bar{\mathbf{x}}_{BA} {}^A\boldsymbol{\omega}_{AN}) \\ -{}^A\boldsymbol{\omega}_{AN} \times {}^N\mathbf{R}_A^T {}^N\mathbf{R}_B^B \boldsymbol{\omega}_{BN} & \text{-----} \end{bmatrix} \\
 + \frac{1}{r} \dot{\mathbf{\Lambda}}^T {}^A\bar{\mathbf{R}}_B (\mathbf{C}_1 \dot{\mathbf{x}}_A + \mathbf{C}_2 \dot{\mathbf{x}}_B) \mathbf{C}_7 &= \frac{r_{wh}}{2} \begin{bmatrix} \frac{d}{b} \cos \varphi_A - \sin \varphi_A & -\frac{d}{b} \cos \varphi_A - \sin \varphi_A \\ \frac{d}{b} \sin \varphi_A + \cos \varphi_A & -\frac{d}{b} \sin \varphi_A + \cos \varphi_A \\ \mathbf{0}_{4 \times 1} & \mathbf{0}_{4 \times 1} \end{bmatrix}, \quad \mathbf{C}_9 = \begin{bmatrix} \mathbf{0}_{3 \times 1} \\ \dot{\mathbf{P}}_B \dot{\boldsymbol{\psi}}_B \end{bmatrix} \\
 {}^A\mathbf{x}_{BA} = {}^N\mathbf{R}_A^T ({}^N\mathbf{x}_{BN} - {}^N\mathbf{x}_{AN}), \quad {}^A\bar{\mathbf{x}}_{BA} &= \begin{bmatrix} 0 & -{}^A x_{BA,z} & {}^A x_{BA,y} \\ {}^A x_{BA,z} & 0 & -{}^A x_{BA,x} \\ -{}^A x_{BA,y} & {}^A x_{BA,x} & 0 \end{bmatrix}, \quad {}^A\bar{\mathbf{R}}_B = \begin{bmatrix} \mathbf{I}_3 & \mathbf{0}_3 \\ \mathbf{0}_3 & {}^N\mathbf{R}_A^T {}^N\mathbf{R}_B \end{bmatrix} \\
 {}^A\bar{\mathbf{W}}_{AN} = \begin{bmatrix} 0 & -\dot{\varphi}_A & 0 \\ \dot{\varphi}_A & 0 & 0 \\ 0 & 0 & 0 \end{bmatrix}, \quad {}^A\bar{\mathbf{W}}_{AN}^2 = \begin{bmatrix} -\dot{\varphi}_A^2 & 0 & 0 \\ 0 & -\dot{\varphi}_A^2 & 0 \\ 0 & 0 & 0 \end{bmatrix}
 \end{aligned}$$

B. Deriving the Dynamic Equations of the Flexible System

The dynamic equations of the system are derived employing the Gibbs–Appell formulation as follows:

$$\left(\frac{\partial S}{\partial \dot{\xi}} \right)^T + \left(\frac{\partial \dot{U}}{\partial \dot{\xi}} \right)^T + \left(\frac{\partial D}{\partial \dot{\xi}} \right)^T = \left(\frac{\partial \dot{W}}{\partial \dot{\xi}} \right)^T \tag{B.1}$$

where ξ is the quasi-velocity vector, S is the acceleration energy or Gibbs function, and \dot{W} is the generalized power of the external forces and torques. \dot{U} and D denote the potential energy rate and the Rayleigh’s function. The Gibbs function of the system S consists of the Gibbs function of the platform, the wheels, the end-effector, and the CDPR motors.

$$\begin{aligned}
 S &= \frac{1}{2} \ddot{\mathbf{x}}_A^T [\mathbf{M}_A] \ddot{\mathbf{x}}_A + \ddot{\mathbf{x}}_A^T \begin{bmatrix} \mathbf{0}_3 \\ \mathbf{I}_3 \end{bmatrix} \left(([\mathbf{0}_3 \quad \mathbf{I}_3] \dot{\mathbf{x}}_A) \times (\mathbf{I}_A [\mathbf{0}_3 \quad \mathbf{I}_3] \dot{\mathbf{x}}_A) \right) \\
 &+ \frac{1}{2} \ddot{\mathbf{x}}_B^T [\mathbf{M}_B] \ddot{\mathbf{x}}_B + \ddot{\mathbf{x}}_B^T \begin{bmatrix} \mathbf{0}_3 \\ \mathbf{I}_3 \end{bmatrix} \left(([\mathbf{0}_3 \quad \mathbf{I}_3] \dot{\mathbf{x}}_B) \times (\mathbf{I}_B [\mathbf{0}_3 \quad \mathbf{I}_3] \dot{\mathbf{x}}_B) \right) \\
 &+ \frac{1}{2} \ddot{\boldsymbol{\theta}}^T \mathbf{I}_w \ddot{\boldsymbol{\theta}} + \frac{1}{2} (\ddot{\boldsymbol{\beta}} + \mathbf{C}_{10} \ddot{\mathbf{x}}_A)^T \mathbf{I}_m (\ddot{\boldsymbol{\beta}} + \mathbf{C}_{10} \ddot{\mathbf{x}}_A)
 \end{aligned} \tag{B.2}$$

where

$$\mathbf{C}_{10} = [\mathbf{0}_{6 \times 5}, \mathbf{1}_{6 \times 1}], \quad [\mathbf{M}_A] = \begin{bmatrix} m_A \mathbf{I}_3 & \mathbf{0}_3 \\ \mathbf{0}_3 & \mathbf{I}_A \end{bmatrix}, \quad [\mathbf{M}_B] = \begin{bmatrix} m_B \mathbf{I}_3 & \mathbf{0}_3 \\ \mathbf{0}_3 & \mathbf{I}_B \end{bmatrix}$$

where m_A and m_B are the platform and the end-effector mass, respectively. The matrices \mathbf{I}_A and \mathbf{I}_B denote the moment of inertia tensors of the platform and the end-effector, respectively. \mathbf{I}_m is the equivalent inertia of the rotating parts of the CDPR’s motors and \mathbf{I}_w is the inertia of the wheels and the connected moving parts of the related motors. The rate of the potential energy due to the cables elasticity and the gravity is obtained as:

$$\begin{aligned}
 \dot{U} &= \Delta \mathbf{q}^T \mathbf{K}(\mathbf{q}_u) \Delta \dot{\mathbf{q}} + \frac{1}{2} \Delta \mathbf{q}^T \dot{\mathbf{K}}(\mathbf{q}_u) \Delta \mathbf{q} - m_{BG} \dot{z} \\
 \mathbf{K}(\mathbf{q}_u) &= \text{diag} \left(\frac{EA}{\mathbf{q}_u} \right)
 \end{aligned} \tag{B.3}$$

where E , A , m_e , and $\Delta \mathbf{q}$ are Young’s modulus, cable section area, cable mass, and the cable elongation due to the elasticity. The cable damping model is proportional. The damped energy is the result of the fast dynamic and corresponds to the rate of the cable length elongation. Therefore, Rayleigh’s function is expressed as:

$$D = \frac{1}{2} \Delta \dot{\mathbf{q}}^T \mathbf{C}_d \Delta \dot{\mathbf{q}}, \quad \text{where: } \mathbf{C}_d(\mathbf{q}_u) = \text{diag} \left(\frac{c_d}{\mathbf{q}_u} \right) \tag{B.4}$$

where c_d is the cable damping coefficient per unit length. The generalized power of the external torques is defined as:

$$\dot{W} = \boldsymbol{\tau}_\beta^T \dot{\boldsymbol{\beta}} + \boldsymbol{\tau}_\theta^T \dot{\boldsymbol{\theta}} \tag{B.5}$$

$\boldsymbol{\tau}_\beta$ and $\boldsymbol{\tau}_\theta$ are the torque vector of the CDPR and the WMR parts of the robot, respectively.

C. Coefficient Matrices in the Rigid Dynamic Equations

In Eq. (22), the mass matrix \mathbf{M} , centrifugal and Coriolis vector \mathbf{C} , gravity vector \mathbf{G} , and the torque coefficient matrix \mathbf{F} are as follows:

$$\begin{aligned} \mathbf{M} &= \begin{bmatrix} \mathbf{m}_{11} & \mathbf{m}_{12} \\ \mathbf{m}_{21} & \mathbf{m}_{22} \end{bmatrix} \\ \mathbf{m}_{11} &= \mathbf{C}_8^T (\mathbf{C}_4^T \mathbf{I}_m \mathbf{C}_4 + [\mathbf{M}_B]) \mathbf{C}_8, \quad \mathbf{m}_{12} = \mathbf{C}_8^T (\mathbf{C}_4^T \mathbf{I}_m (\mathbf{C}_3 + \mathbf{C}_{10}) \mathbf{C}_6), \\ \mathbf{m}_{21} &= (\mathbf{C}_8^T (\mathbf{C}_4^T \mathbf{I}_m (\mathbf{C}_3 + \mathbf{C}_{10}) \mathbf{C}_6))^T \\ \mathbf{m}_{22} &= \mathbf{C}_6^T [\mathbf{M}_A] \mathbf{C}_6 + \mathbf{C}_6^T (\mathbf{C}_3 + \mathbf{C}_{10})^T \mathbf{I}_m (\mathbf{C}_3 + \mathbf{C}_{10}) \mathbf{C}_6 + \mathbf{I}_w \end{aligned} \tag{C.1}$$

$$\begin{aligned} \mathbf{C} &= \begin{bmatrix} \mathbf{c}_{11} \\ \mathbf{c}_{21} \end{bmatrix} \\ \mathbf{c}_{11} &= \mathbf{C}_8^T ((\mathbf{C}_4^T \mathbf{I}_m \mathbf{C}_4 + [\mathbf{M}_B]) \mathbf{C}_9 + \mathbf{C}_4^T \mathbf{I}_m ((\mathbf{C}_3 + \mathbf{C}_{10}) \mathbf{C}_7 \dot{\boldsymbol{\theta}} + \mathbf{C}_5)) + \begin{bmatrix} \mathbf{0}_{3 \times 1} \\ \mathbf{P}_B^T (\mathbf{P}_B \dot{\boldsymbol{\psi}}_B \times \mathbf{I}_B \mathbf{P}_B \dot{\boldsymbol{\psi}}_B) \end{bmatrix} \\ \mathbf{c}_{21} &= (\mathbf{C}_6^T (\mathbf{C}_3 + \mathbf{C}_{10})^T \mathbf{I}_m \mathbf{C}_4) \mathbf{C}_9 + \mathbf{C}_6^T [\mathbf{M}_A] \mathbf{C}_7 \dot{\boldsymbol{\theta}} + \mathbf{C}_6^T (\mathbf{C}_3 + \mathbf{C}_{10})^T \mathbf{I}_m ((\mathbf{C}_3 + \mathbf{C}_{10}) \mathbf{C}_7 \dot{\boldsymbol{\theta}} + \mathbf{C}_5) \\ &\quad + \mathbf{C}_6^T \begin{bmatrix} \mathbf{0}_{3 \times 1} \\ \mathbf{P}_A \dot{\boldsymbol{\psi}}_A \times \mathbf{I}_A \mathbf{P}_A \dot{\boldsymbol{\psi}}_A \end{bmatrix} \end{aligned} \tag{C.2}$$

$$\mathbf{G} = [\mathbf{M}_B] \begin{bmatrix} \mathbf{0}_{2 \times 1} \\ -g \\ \mathbf{0}_{5 \times 1} \end{bmatrix} \tag{C.3}$$

$$\mathbf{F} = \begin{bmatrix} \frac{1}{r} \mathbf{C}_8^T \mathbf{C}_2^T \mathbf{A}^T \bar{\mathbf{R}}_B^T \boldsymbol{\Lambda} & \mathbf{0}_2 \\ \frac{1}{r} \mathbf{C}_6^T \mathbf{C}_1^T \mathbf{A}^T \bar{\mathbf{R}}_B^T \boldsymbol{\Lambda} & \mathbf{I}_2 \end{bmatrix} \tag{C.4}$$

D. Torques Applied to the CDPR and the Wheels Motors

Figure D.1 shows the calculated LQR torque for the wheel motors in Section 5.1. This torque is converted to the required voltage with saturation limit. In Section 5.2, the motor torques applied on the CDPR are demonstrated in Figs. D.2, D.3, and D.4.

It can be seen that the required torque of the CDPR and platform are not saturated. However, as shown in Fig. 16, after conversion to the voltage and passing through the filter, the wheel control input is saturated about the middle of the tracking.

Also, the torques related to the simulation in Section 6 are shown in Figs. D.5, D.6, D.7, and D.8. The fluctuation of the torques shown in these figures is contributed to the end-effector motion in z direction.

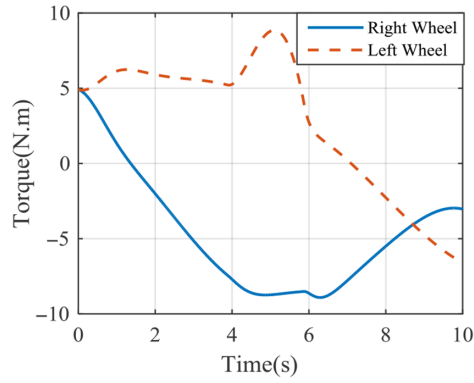


Fig. D.1. The wheel motor torques.

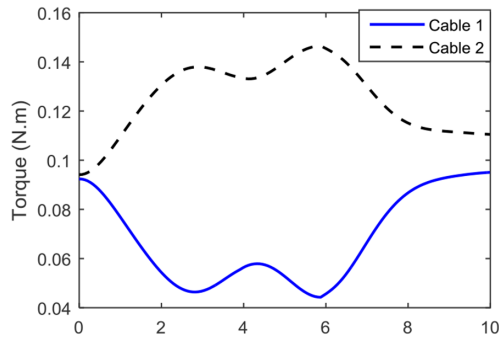


Fig. D.2. The first and second cable motor torques.

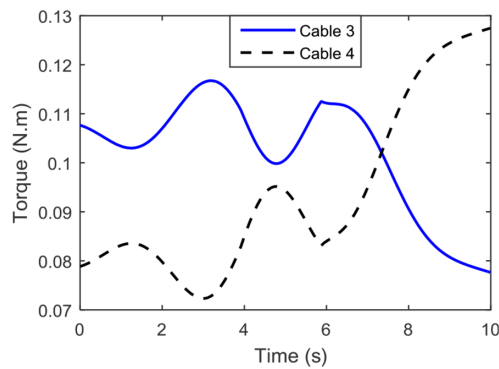


Fig. D.3. The third and fourth cable motor torques.

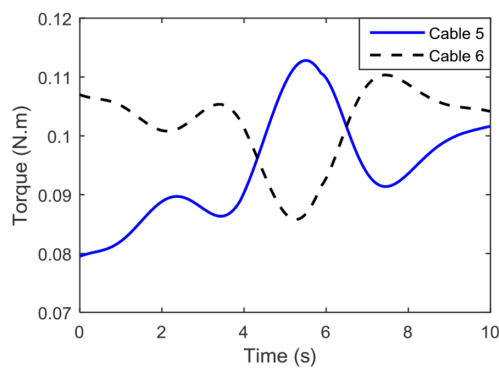


Fig. D.4. The fifth and sixth motor torques.

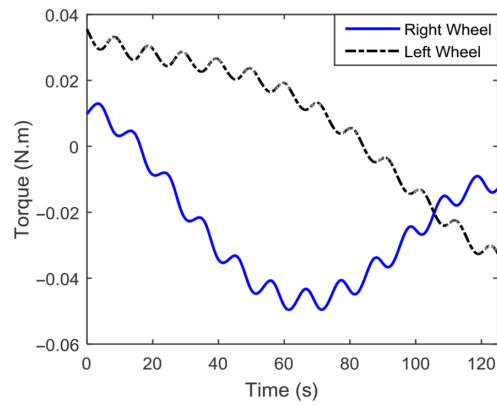


Fig. D.5. The wheel motor torques.

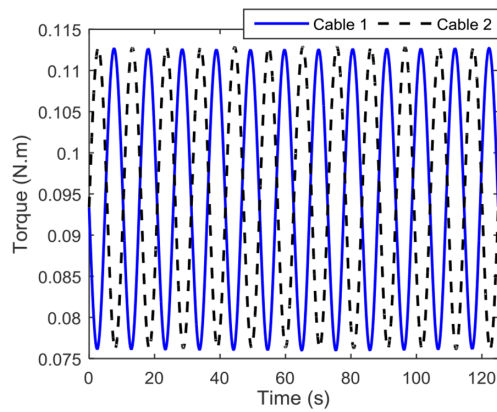


Fig. D.6. The first and second motor torques.

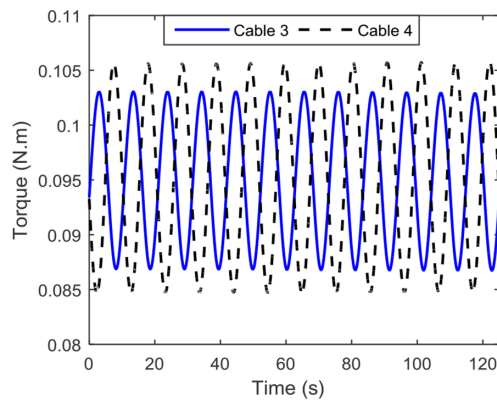


Fig. D.7. The third and fourth motor torques.

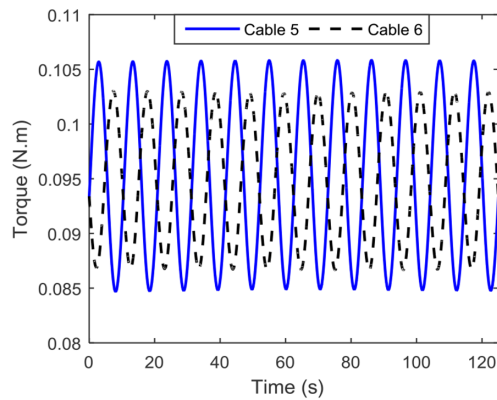


Fig. D.8. The fifth and sixth motor torques.